UNIVERSITY OF CALIFORNIA,
IRVINE

Single-Nanoparticle Microscopy of DNA-Incorporated Hydrogel Nanoparticles

DISSERTATION

submitted in partial satisfaction of the requirements
for the degree of

DOCTOR OF PHILOSOPHY

in Chemistry

by

Brandon Marcellus Matthews

Dissertation Committee:
Professor Robert M. Corn, Chair
Professor Rachel W. Martin
Professor Reginald M. Penner

2019

DEDICATION

To

my mom Alicia and my grandma Patsy
ace boon coons for life

TABLE OF CONTENTS

LIST OF FIGURES

LIST OF TABLES

ACKNOWLEDGMENTS

There's whole host of people, events, and things that made me finally get to this endpoint of my life, and onto the precipice of another. As much as I would thoroughly enjoy breaking down every instance of opportunities of growth and self-determination, for professional brevity sake, I'll lead off with a simple thank you. A collective thank you. For the sheer number of hours, days, and weeks of memories and changes as I finally finish this bridge over troubled waters. I owe my saving grace to so many amazing people in my life, some I've known forever in a day, and others who've become permanent fixtures in my life from these last five years.

Starting in house: the Corn group. I would like to acknowledge my PI Rob Corn. To past and current group members, thank you as well. Shout out to Cabo Cantina for making us all click together. Kellen, I've had the extreme pleasure of sharing half a brain with you over our graduate career (and beyond, since, you know). I can honestly say you've been a major supporting and motivating force getting me through everything, and still I expect Milkbox runs going forward. Or just really any boba run, honestly.

To my other girls, Brit and 'Lana, wow we did it. Go us. I hope there's a point in the future we're we can all at the very least be on the same coast again, but until that happens again (and it will) we got 5+ years of group text, hang outs, bread boxes, and wine nights of a foundation. Ro (and certainly by extension David and Avs) I could not have been more blessed and honored in you kidnapping me the first day we met for a solid five hours. Danielle, thank you for the constant reminders that I, too, deserve a seat at the table. Phong (aka B.G.) you've been such a fantastic grounding force of goofy.

To my family, thank you for taking me as I am and for encouraging me to be the best nerd possible. To my mom Alicia, we made it. I couldn't have done any of this without you and

your love. To my grandmother Patsy, thank you for being the other constant force in my life. To my brothers Braxton and Brenton, thank you for holding it down all these years. And to the rest of the Jones clan, through it all, thick and thin, we outchea.

To my found family, thank you. We have on average 10+ years of bonds mixing and matching and strengthening. WHIPJOT got 12 straight years (thank god for the growth). Marky, Bates, Linds – we all have come a long way since Sra. Aquino's class. David thank you for staying on my neck in the best possible way. Sally-from-the-valley, thank you for being my big sis for all these years. Tim, thank you for having mostly matching taste. Your support means so much and I thank you all for being a part of my life.

This work presented in this dissertation was supported by the National Science Foundation through grant CHE-1807317 and the National Institute of Health through grant R01-GM059622.

.

CURRICULUM VITAE

Brandon Matthews

Education

University of California, Irvine (Irvine, CA)
Ph.D., Chemistry, 2019
Advisor: Professor Robert Corn

University of California, Los Angeles (Los Angeles, CA)
B.S., Chemistry, 2014

Professional Experience

Graduate Student Researcher
Department of Chemistry, University of California, Irvine (Irvine, CA), 2014-2019

Teaching Assistant
Department of Chemistry, University of California, Irvine (Irvine, CA), 2014-2017

Undergraduate Student Researcher
Department of Chemistry, University of California, Los Angeles (Los Angeles, CA), 2012-2014

Publications

H. Aoki, R. M. Corn, **B. M. Matthews.** (2019) MicroRNA detection on microsensor arrays by SPR imaging measurements with enzymatic signal enhancement. Biosens. Bioelectron. *Submitted.*

B. M. Matthews, A. M. Maley, K. M. Kartub, R. M. Corn. Characterizing the Incorporation of DNA into Single NIPAM Hydrogel Nanoparticles with Surface Plasmon Resonance Imaging Measurements. J. Phys. Chem. C. 2019, 123 (10), 6090-6096.

J. P. Kenison, A. Fast, **B. M. Matthews**, R. M. Corn, E. O. Potma. Particle sensing with confined optical field enhanced fluorescence emission (Cofefe). Optics Express, 2018, 26 (10), 12959-12969.

ABSTRACT OF THE DISSERTATION

Single-Nanoparticle Microscopy of DNA-Incorporated Hydrogel Nanoparticles

By

Brandon Marcellus Matthews

Doctor of Philosophy in Chemistry

University of California, Irvine, 2019

Professor Robert M. Corn, Chair

This dissertation is the cumulative work towards the development of bioactive hydrogel nanoparticles by way of DNA incorporation. First, a collection of orthogonal DNA sequences is fabricated and binding coefficients quantified via surface plasmon resonance imaging (SPRI). Then, using a sample sequence from the collection, the DNA is polymerized into the backbone of hydrogel nanoparticles (HNPs) to be characterized by single-nanoparticle SPRI microscopy as surface adsorption measurements to gold thin-films. The SPRI responses, $\Delta\%R_{NP}$, from several hundred nanoparticle adsorption events are used to generate frequency distribution histograms that characterize the nanoparticle size, composition, and bioactivity through complementary DNA hybridization and enzymatic-induced hydrolysis. These analyses reveal a dependence on the base sequence to aid in the incorporation of DNA into the HNPs. Lastly, DNA incorporation is further elaborated upon by the formation of nanocomposite HNPs, wherein the magnetic nanoparticle ferrite is present during DNA-HNP formation, alluding to a preferential covalent incorporation of DNA over that of ferrite nanoparticles as characterized by SPRI microscopy.

Chapter 1

Introduction

1.1 Dissertation Overview

Nanomaterials have been studied and characterized for a wide use of fields. More recently, these nanomaterials have seen increased usage in the field of nanomedicine, ranging from disease detection via biosensing, or controlled-release drug delivery scaffolds.[1-6] More specifically, polymer-based nanoparticles provide an interesting avenue given their ability to be functionalized with bioactive components, forming novel biofunctionalized scaffolds,[7-8] their chemical inertness in biological samples,[9] and their sensing capabilities combined with other types of nanomaterials[10], inorganic or metallic in nature.[11-12] Yet, more traditional methods of nanoparticle characterization either are most normalized for bulk samples, or when extending to the single-nanoparticle level, degrade or alter the sample itself, restricting *in-situ* characterization.[13-15] In this dissertation, we describe how near-infrared surface plasmon resonance imaging (SPRI) microscopy is an interesting alternative that permits the *in-situ* characterization of biofunctionalized hydrogel nanoparticles. In Chapter 2, we fabricate orthogonal DNA sequences and quantitate their binding efficiencies. In Chapter 3, we synthesis DNA-incorporated hydrogel nanoparticles using a DNA sequence elaborated upon in the previous chapter. Finally, in Chapter 4, we construct nanocomposite hydrogel nanoparticles using both DNA polymerization and ferrite entrapment within the polymer matrix.

1.2 Surface Plasmon Resonance Imaging

SPRI is a surface sensitive technique that measures changes of the local refractive index at the metal/dielectric interface.[16] An example of this label-free detection method is shown in Figure 1.1, and most commonly used for detection between biological molecules, such as complementary hybridization between oligonucleotides or protein capture by a tethered molecular probe.[17] When employing SPRI, *p*-polarized light is collimated and shown incident

onto a coupled prism/thin gold film interface in the Kretschmann configuration. This specific resonance condition creates surface plasmon polaritons (SPPs), which exponentially decay several hundred nanometers into the dielectric (water or air), giving SPRI its surface sensitivity. The angle of this incidence is θ_{SPR}. These SPP waves are very sensitive to the local refractive index of the dielectric, and thus, upon binding of a target analyte, the resonance conditions change, shifting θ_{SPR}. Figure 1.2 outlines the reflectivity curve for a 45 nm Au surface before (red curve) and after (blue curve) molecular adsorption as predicted by the Fresnel equations. Measurements are made at a fixed angle (θ_{SPRI}), approximately 30% off the θ_{SPR}, which is the steepest part of the reflectivity curve, allowing for enhanced sensitivity of detection. The dotted black line is the tracking of the observed reflectivity change (Δ%R) as molecules adsorb to the surface.

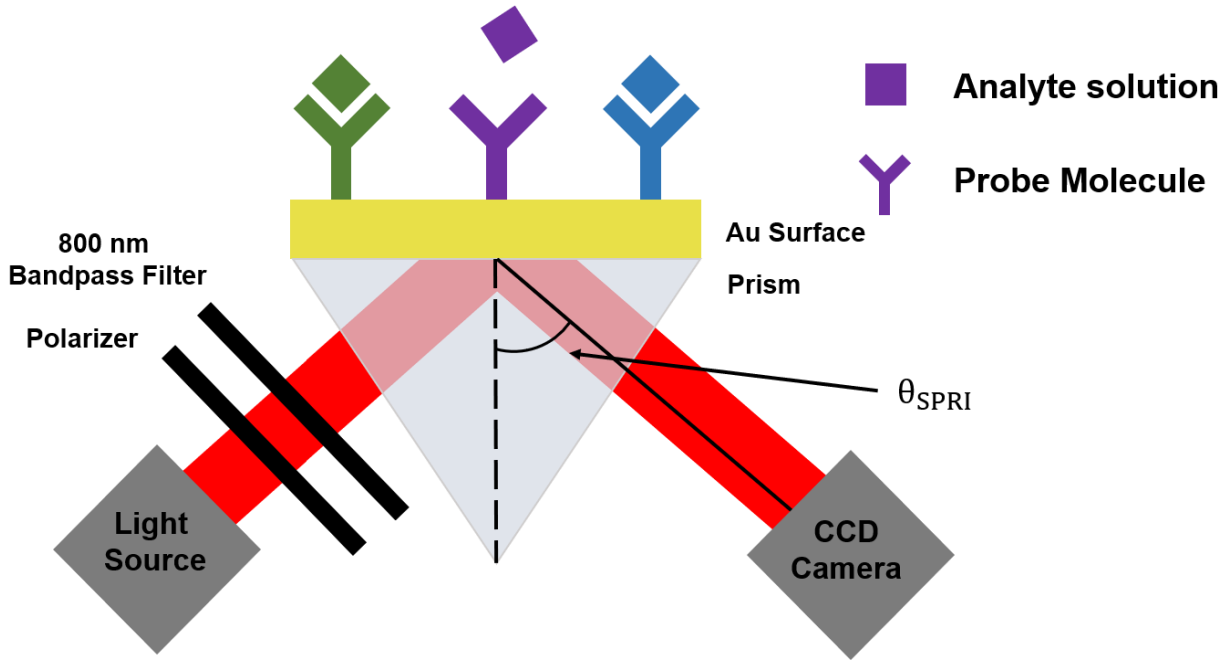

Figure 1.1: Schematic of SPR imager. *P*-polarized light collimated to 800 nm is reflected off the back of a gold thin-film surface coupled to a high refractive index prism. The reflected light is captured by a CCD camera. When surface probe molecules capture target analytes, a shift in reflectivity occurs.

This detection method encourages the multiplexed detection of bioaffinity adsorptions simultaneously.[18] Gold film surfaces are especially attractive due to it being both biologically inert and due to the number of biofunctional methods that have been developed for successful bioaffinity adsorptions.[19] Direct detection of these adsorption events can readily be tracked at nanomolar concentrations, and potentially into the femtomolar concentrations through enzyme chemistries such as ligases, nucleases, and polymerases, as well as nanoparticle signal enhancements.[20]

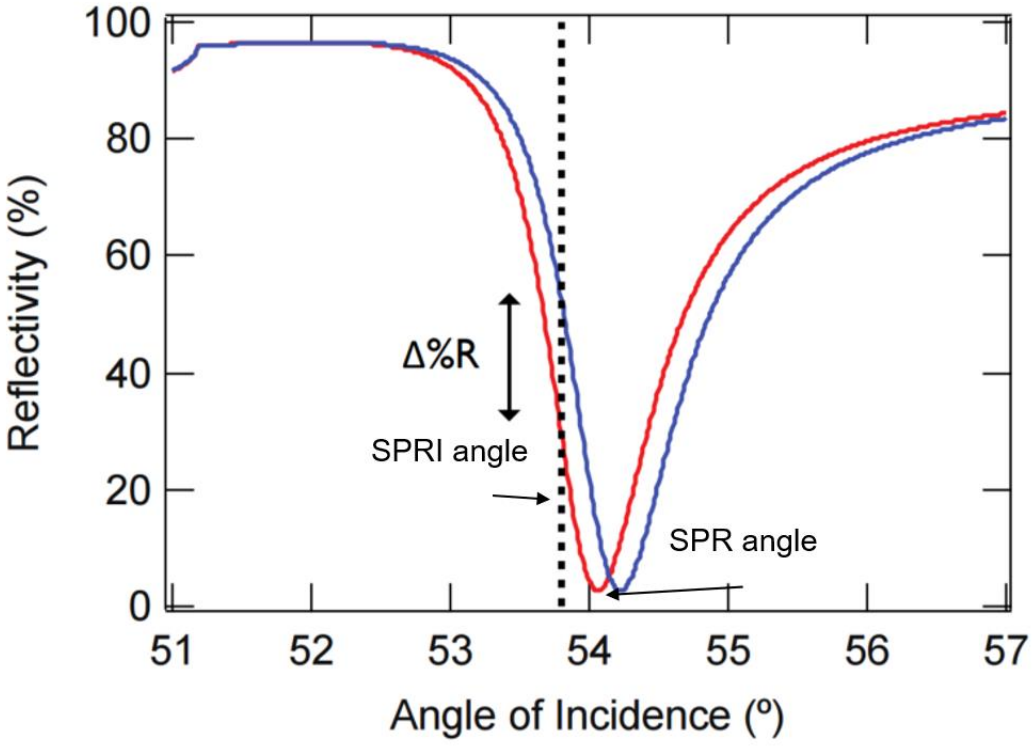

Figure 1.2: SPR reflectivity curve for 45 nm gold film on a highly reflective glass (red curve). When target molecules absorb to the surface, a shift in reflectivity is observed (blue curve), resulting in an increase in reflectivity (black dotted line).

Chapter 2 of this dissertation uses SPRI to explore 30mer orthogonal DNA sequences and quantifying their binding coefficients at equilibrium. A library of DNA sequences is created for future use in multiplexed detection in microarray fabrication. The four oligonucleotides

sequences are first examined to demonstrate orthogonality to each other and complementary sequences. This is done by systematically exposing microarrays with immobilized DNA on the surface to a single DNA at a time and tracking any adsorption that occurs. Following, each sequence is hybridized to its complement over a range of concentrations to determine the equilibrium constant for each hybridization interaction: one from real-time kinetic curves, and one from thermodynamic equilibrium. Even with different analytical examinations, the resulting equilibrium constants are shown to be similar to each other.

1.3 Single-Nanoparticle Surface Plasmon Resonance Imaging

Although most SPRI measurements are conducted on the macroscale by monitoring tens to hundreds of sensor elements simultaneously, there has been increased interest in using microscope objectives for high-resolution SPRI measurements. Initially demonstrated by Zybin and Tao in 2010,[21-22] SPR microscopes have been used to study individual nanoparticles, proteins, viruses, cells, and liposomes.[23-26] Our lab's construction of a near-infrared SPRI microscope setup is demonstrated in Figure 1.3, built into the frame of an inverted fluorescence microscope. In place of a prism of more traditional SPR imaging measurements, a 100× high numerical aperture oil immersion objective lens is used to couple to a gold-coated coverslip. An 814 nm laser is used to excite SPPs and is used in favor of greater sensitivity over visible light. The laser is expanded and collimated using spatial filter, then passed through a polarizer to be focused (f = 200 mm) onto the back focal pane of 1.49 NA microscope objective. A gold coated knife edge mirror is mounted on an X – Y micrometer and used to focus light upward into the edge of the objective, controlling the light's angle of incidence. The reflected light is passed through other edge of the objective and is collected by a CMOS camera.

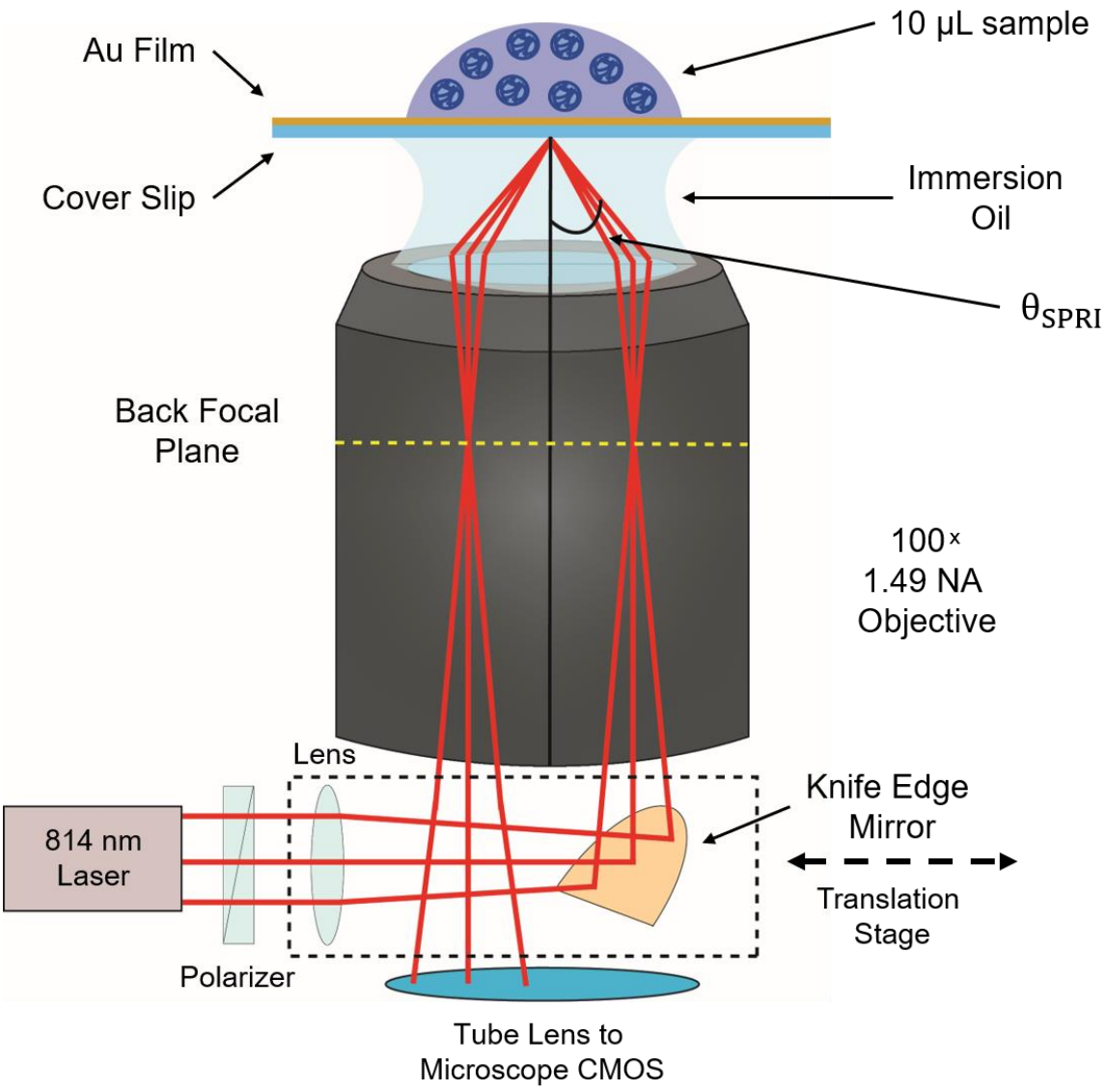

Figure 1.3: Schematic diagram of the single-nanoparticle SPRI microscope. A gold-coated knife edge mirror is utilized to direct the collimated 814 nm p-polarized light through the microscope objective and onto the back of a gold-coated coverslip. The reflected image is captured by a CMOS camera.

To image *in situ* adsorption of individual nanoparticles, we analyze the point diffractions that arise from the SPRI differential reflectivity images. Each collection of images is taken over a ten-minute time frame, wherein each image is captured every three seconds. Differential reflectivity images are then created by sequentially subtracting from each other; nanoparticles

will only appear upon initial adsorption to the surface by electrostatic interactions. By employing frame-by-frame difference imaging, we eliminate also the need to observe long-term intensity fluctuations. When a particle interacts with the gold thin film surface, it interacts with the propagating SPP waves. The integrated refractive index of the particle functions as a point diffraction, which in turn yields the diffraction pattern that appears in the reflectivity images.

Figure 1.4 shows the adsorption of 200 nm hydrogel nanoparticles. Here, nanoparticle adsorption events can be tracked and mapped to realize real-time binding kinetics from the differential reflectivity images. When a nanoparticle adsorbs to the surface, a high intensity point diffraction is documented and tracked. For each type of particle-surface interaction, binding curves can be realized, as shown by Halpern using complementary DNA sequences between gold nanoparticles and the gold film surface.[23] Adsorption rates are dependent on the concentration of nanoparticles.

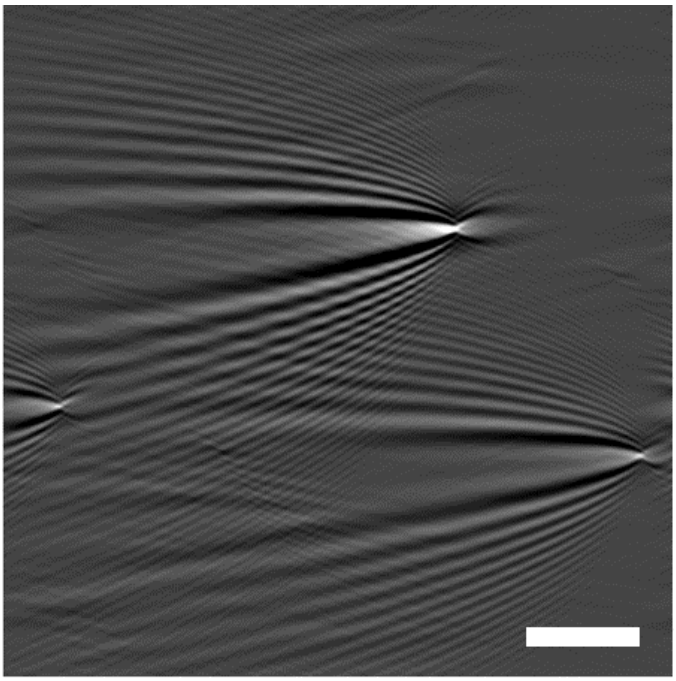

Figure 1.4: Fourier-filtered differential SPRI reflectivity image from the absorption of DNA-incorporated hydrogel nanoparticles onto a 45 nm gold-film surface. The total image area is 58.5 μm × 58.5 μm, and the scale bar is 10 μm.

1.4 Bioactive Polymer Nanoparticle Characterization

Recent endeavors in our lab focus on the examination of protein and polymeric nanoparticles. While more typical electron microscopies are effective for metallic nanoparticles, protein and polymer-based nanoparticles prove to be challenging to characterize at the single-nanoparticle level.[27-28] SPRI microscopy provides a suitable alternative to examine *in-situ* characterization of protein and polymer nanoparticles based on changes in refractive index. It is an additionally attractive avenue of characterization as it can detect unlabeled uptake into its porous nanostructure.

Previously, our group has shown target specific uptake when using *N*-isopropylacrylamide (NIPAm) HNPs via hydrophobic and electrostatic interactions. When examining mannose-incorporated HNPs uptake of concanavalin A (ConA), it was shown that the distribution of $\Delta\%R_{NP}$ values can be tracked and quantitated using SPRI microscopy, indicating both uptake and cross-linkage between particles.[29] Later studies used $\Delta\%R_{NP}$ distributions to characterize size distributions, and monitor nanoparticle aggregation driven by bioaffinity interactions between peptides and proteins.[30]

Chapter 3 explores SPRI microscopy's use with DNA-incorporated hydrogel nanoparticles. Here, various DNA sequences are polymerized into the polymer backbone, forming a bioactive hydrogel that was shown to be selective to both hybridization capture with complementary pairing, as well as selective activity to enzyme chemistries. Single-nanoparticle measurements are taken to show variation of DNA effects on synthesis, showing a ten-fold increase in $\Delta\%R_{NP}$ when comparing HNPs to DNA-HNPs signal averages, emphasizing the effect of DNA incorporation through the formation of adducts via Michael addition. A binding

curve mapped from a range of complementary DNA also is generated to yield the equilibrium constant of DNA hybridization within the hydrogel.

While continuing to use DNA-HNPs, Chapter 4 explores the formation of composite hydrogel nanoparticles via synthesis in the presence of magnetic nanoparticles. Several batches of HNPs are synthesized in the presence of DNA and/or magnetic nanoparticles. For HNPs with just magnetic nanoparticles, a drastic increase in average $\Delta\%R_{NP}$ is observed due to the clustering of the smaller nanoparticles within the polymer nanoparticle. However, with the addition of DNA in the presence of the magnets, the signal drops, demonstrating a preference of covalently incorporating the DNA sequence over minimizing charge repulsions between the non-covalently incorporated magnetic nanoparticle and the HNP. This effect is further exaggerated when hybridizing in complementary DNA, ejecting the magnetic nanoparticles out and further decreasing the $\Delta\%R_{NP}$ average signal. However, this process also confirmed bioavailablity of the composite nanoparticle even in the presence of biologically inert species. This examination is further corroborated using cryo-TEM measurements.

1.5 References

1. McKeague, M.; DeRosa, M. C., Challenges and Opportunities for Small Molecule Aptamer Development. *J. Nuc. Acid* **2012**, 2012, 20.

2. Li, Y.; Lee, H. J.; Corn, R. M., Detection of Protein Biomarkers Using RNA Aptamer Microarrays and Enzymatically Amplified Surface Plasmon Resonance Imaging. *Anal. Chem.* **2007,** *79* (3), 1082-1088.

3. Xu, F.; Dong, H.; Cao, Y.; Lu, H.; Meng, X.; Dai, W.; Zhang, X.; Al-Ghanim, K. A.; Mahboob, S., Ultrasensitive and Multiple Disease-Related MicroRNA Detection Based on

Tetrahedral DNA Nanostructures and Duplex-Specific Nuclease-Assisted Signal Amplification. *ACS Appl. Mater. Interfaces* **2016,** *8* (49), 33499-33505.

4. Carrascosa, L. G.; Huertas, C. S.; Lechuga, L. M., Prospects of optical biosensors for emerging label-free RNA analysis. *TrAC, Trends Anal. Chem.* **2016,** *80*, 177-189.

5. Kahn, J. S.; Hu, Y.; Willner, I., Stimuli-Responsive DNA-Based Hydrogels: From Basic Principles to Applications. *Acc. Chem. Res.* **2017,** *50* (4), 680-690.

6. Wang, D.; Hu, Y.; Liu, P.; Luo, D., Bioresponsive DNA Hydrogels: Beyond the Conventional Stimuli Responsiveness. *Acc. Chem. Res.* **2017,** *50* (4), 733-739.

7. Plamper, F. A.; Richtering, W., Functional Microgels and Microgel Systems. *Acc. Chem. Res.* **2017,** *50* (2), 131-140.

8. Lopez, A.; Liu, J., Self-Assembly of Nucleobase, Nucleoside and Nucleotide Coordination Polymers: From Synthesis to Applications. *ChemNanoMat.* **2017,** *3* (10), 670-684.

9. Peppas, N. A.; Hilt, J. Z.; Khademhosseini, A.; Langer, R., Hydrogels in Biology and Medicine: From Molecular Principles to Bionanotechnology. *Adv. Mater.* **2006,** *18* (11), 1345-1360.

10. Carvalho, W. S. P.; Wei, M.; Ikpo, N.; Gao, Y.; Serpe, M. J., Polymer-Based Technologies for Sensing Applications. *Anal. Chem.* **2018,** *90* (1), 459-479.

11. Li, W.; Hu, L.; Zhu, J.; Li, D.; Luan, Y.; Xu, W.; Serpe, M. J., Comparison of the Responsivity of Solution-Suspended and Surface-Bound Poly(N-isopropylacrylamide)-Based Microgels for Sensing Applications. *ACS Appl. Mater. Interfaces.* **2017,** *9* (31), 26539-26548.

12. Lilienthal, S.; Shpilt, Z.; Wang, F.; Orbach, R.; Willner, I., Programmed DNAzyme-Triggered Dissolution of DNA-Based Hydrogels: Means for Controlled Release of Biocatalysts

and for the Activation of Enzyme Cascades. *ACS Appl. Mater. Interfaces.* **2015,** *7* (16), 8923-8931.

13. Cho, E. J.; Holback, H.; Liu, K. C.; Abouelmagd, S. A.; Park, J.; Yeo, Y., Nanoparticle characterization: state of the art, challenges, and emerging technologies. *Mol. Pharm.* **2013,** *10* (6), 2093-2110.

14. Ballauff, M.; Lu, Y., "Smart" nanoparticles: Preparation, characterization and applications. *Polymer* **2007,** *48* (7), 1815-1823.

15. Till, U.; Gaucher-Delmas, M.; Saint-Aguet, P.; Hamon, G.; Marty, J. D.; Chassenieux, C.; Payre, B.; Goudouneche, D.; Mingotaud, A. F.; Violleau, F., Asymmetrical flow field-flow fractionation with multi-angle light scattering and quasi-elastic light scattering for characterization of polymersomes: comparison with classical techniques. *Anal. Bioanal. Chem.* **2014,** *406* (30), 7841-7853.

16. Masson, J.-F., Surface Plasmon Resonance Clinical Biosensors for Medical Diagnostics. *ACS Sens.* **2017,** *2* (1), 16-30.

17. Smith, E. A.; Corn, R. M., Surface plasmon resonance imaging as a tool to monitor biomolecular interactions in an array based format. *Appl. Spectrosc.* **2003,** *57* (11), 320A-332A.

18. Sendroiu, I. E.; Gifford, L. K.; Luptak, A.; Corn, R. M., Ultrasensitive DNA Microarray Biosensing via in Situ RNA Transcription-Based Amplification and Nanoparticle-Enhanced SPR Imaging. *J. Am. Chem. Soc.* **2011,** *133* (12), 4271-4273.

19. Chen, Y. L.; Nguyen, A.; Niu, L. F.; Corn, R. M., Fabrication of DNA Microarrays with Poly(L-glutamic acid) Monolayers on Gold Substrates for SPR Imaging Measurements. *Langmuir* **2009,** *25* (9), 5054-5060.

20. Fasoli, J. B.; Corn, R. M., Surface Enzyme Chemistries for Ultrasensitive Microarray Biosensing with SPR Imaging. *Langmuir* **2015,** *31* (35), 9527-9536.

21. Zybin, A.; Kuritsyn, Y. A.; Gurevich, E. L.; Temchura, V. V.; Uberla, K.; Niemax, K., Real-time Detection of Single Immobilized Nanoparticles by Surface Plasmon Resonance Imaging. *Plasmonics* **2010,** *5* (1), 31-35.

22. Wang, S.; Shan, X.; Patel, U.; Huang, X.; Lu, J.; Li, J.; Tao, N., Label-Free Imaging, Detection, and Mass Measurement of Single Viruses by Surface Plasmon Resonance. *Proc. Natl. Acad. Sci. U. S. A.* **2010,** *107* (37), 16028-16032.

23. Halpern, A. R.; Wood, J. B.; Wang, Y.; Corn, R. M., Single-Nanoparticle Near-Infrared Surface Plasmon Resonance Microscopy for Real-Time Measurements of DNA Hybridization Adsorption. *ACS Nano* **2014,** *8* (1), 1022-1030.

24. Cho, K.; Fasoli, J. B.; Yoshimatsu, K.; Shea, K. J.; Corn, R. M., Measuring Melittin Uptake into Hydrogel Nanoparticles with Near-Infrared Single Nanoparticle Surface Plasmon Resonance Microscopy. *Anal. Chem.* **2015,** *87* (9), 4973-4979.

25. Viitala, L.; Maley, A. M.; Fung, H. W. M.; Corn, R. M.; Viitala, T.; Murtomaki, L., Surface Plasmon Resonance Imaging Microscopy of Liposomes and Liposome-Encapsulated Gold Nanoparticles. *J. Phy. Chem. C.* **2016,** *120* (45), 25958-25966.

26. Wang, W.; Foley, K.; Shan, X.; Wang, S.; Eaton, S.; Nagaraj, V. J.; Wiktor, P.; Patel, U.; Tao, N., Single Cells and Intracellular Processes Studied by a Plasmonic-Based Electrochemical Impedance Microscopy. *Nat. Chem.* **2011,** *3* (3), 249-255.

27. Crut, A.; Maioli, P.; Del Fatti, N.; Vallee, F., Optical Absorption and Scattering Spectroscopies of Single Nano-Objects. *Chem. Soc. Rev.* **2014,** *43* (11), 3921-3956.

28. Crut, A.; Maioli, P.; Vallee, F.; Del Fatti, N., Linear and Ultrafast Nonlinear Plasmonics of Single Nano-Objects. *J. Phys. Condens. Matter.* **2017,** *29* (12), 123002.

29. Maley, A. M.; Terada, Y.; Onogi, S.; Shea, K. J.; Miura, Y.; Corn, R. M., Measuring Protein Binding to Individual Hydrogel Nanoparticles with Single-Nanoparticle Surface Plasmon Resonance Imaging Microscopy. *J. Phys. Chem. C.* **2016,** *120* (30), 16843-16849.

30. Maley, A. M.; Lu, G. J.; Shapiro, M. G.; Corn, R. M., Characterizing Single Polymeric and Protein Nanoparticles with Surface Plasmon Resonance Imaging Measurements. *ACS Nano* **2017,** *11* (7), 7447-7456.

Chapter 2

Real-Time SPRI Measurements for the Determination of Complementary DNA Adsorption/Desorption Kinetics within an Orthogonal DNA Library

2.1 Introduction

Multiplexed biosensing arrays continue to be a rapid and inexpensive analytical tool used to perform large-scale biomarker detection within a single experiment.[1-5] These arrays can be quite large, on the order of tens to thousands of individual elements, to detect multiple proteins or DNAs.[6-9] Smaller microarrays typically call for more specific biosensing and bioaffinity interaction studies.[10-13] Specifically, DNA-based microarrays are an attractive avenue for multiplexed detection due to the wide range of attachment chemistries that can be employed to immobilize DNA to a surface sensor.[14-15] Additionally, the use of DNA-based detection methods allows for a variety of direct microarray detection, as numerous techniques can assist in detection sensitivity and selection[8, 16], sensor regeneration[17], or signal amplification through the use of enzyme chemistries.[9, 18-19]

In particular, self-assembled microarrays make full use of DNA-based detection sensors.[16-17, 20] Here, detection elements can be fabricated on-chip that retain spatial selectivity and efficiency; this is especially important when working with probe molecules that have limited or decreased function when fabricated in open air. DNA sequences that are orthogonal to each other on a single chip can readily and independently form a complex array of detector elements unique to a target, removing the need for spotting and purification. Length variance for the DNA anchor can also be reflected in its final application, with short strands used for detections like microRNA, and longer sequences acting as single-capture aptamers, or capture of its complement to function as a building scaffold for sandwich assays.

Surface plasmon resonance imaging (SPRI) is a label-free, optical sensing method that can detect the adsorption of molecules to a surface.[21-22] SPRI measurements track the changes in reflectivity as analytes adsorb to the surface and can quantitate the interaction between

biomolecules without alternating or chemically modifying them. This is especially useful when detecting highly sensitive targets. Dictated by biorecognition events between probe and target analyte, SPRI can also effectively monitor scores of bioaffinity interactions while simultaneously tracking multiplexed kinetic measurements of target-analyte interactions via ensemble measurements.[10-11]

In this chapter, a DNA library was manufactured and tested for potential spatial orthogonality by comparing complementary sequence hybridization. These interactions were tracked and analyzed using SPRI over a range of concentrations. From these measurements, the binding constants of duplex formation were found by both real-time adsorption kinetics and by Langmuir isotherm measurements.

2.2 Methods and Materials

2.2.1 Substrate Preparation

SF-10 (18 x 18 mm^2; Schott Glass, Mainz, Germany) substrates were used to create SPRI microarrays as outlined in a previous publication.[14] First, glass slides were washed with EtOH/nanopore water followed by oxygen plasma cleaning for 5 min. Then, substrates were prepared by thermally evaporating (Denton DV 502-A evaporator) 45 nm of gold, with 1 nm of chromium underneath as an adhesion layer onto glass slides, using a mask that results in 16, 1 mm diameter gold film spots, with a distance center to center of 1.5 mm.

To prepare the surface to ssDNA monolayer formation, slides were immersed in a 1 mM 11-amino-1-undecanthiol hydrochloride (MUAM) (Dojindo, Japan) ethanolic solution overnight. Next, poly(L-glutamic acid) sodium salt (MW = 50 000 – 100 000) (pGlu) (Sigma Aldrich, Inc., St. Louis, MO) was permitted to form a monolayer by immersion in a 2 mg/mL pGlu solution in PBS 1x (pH 7.4) buffer for 1 h. To covalently attach DNA probes to the surface, 250 µM amine-

modified ssDNA solution (Integrated DNA Technologies, Coralville, IA) in PBS buffer that also contained 75 mM 1-ethyl-3-(3-(dimethylamino)proply)cabodiimide) (EDC) and 15 mM *N*-hydroxylsulfouccinimide (NHSS) (both Pierce, Dallas, TX) were spotted onto the gold film spots using 0.5 µL solution for 4 h. Each step was followed by a rinsing step and drying under nitrogen stream.

2.2.2 SPR Imaging Measurements

For SPRI measurements, an SPR imager (GWC Technologies) was employed. In real-time, regions of interest were selected on gold film spots to perform ensemble tracking measurements. Initial preparation began by flowing buffer solution through tubing while calibration of imager performed. Collimated *p*-polarized light impinges onto a prism/thin gold film/flow cell assembly at a fixed incident angle of ~30% reflectivity. The reflected light is then passed through a narrow band-pass filter (830 nm) and collected with a CCD camera. Differential images were taken averaging 5 frames at a time, at 3 sec intervals. All SPR images were collected using the software package Digital Optics V++ 4.0. All SPRI experiments were performed under equilibrium conditions. To check for orthogonality between selected DNA sequences, arrays were made as demonstrated in Figure 2.1. Once a library was made of the four DNA sequences and their complements, hybridization data was collected. Complementary DNA was flowed over the DNA array over a range of concentrations, going from 10 to 300 nM.

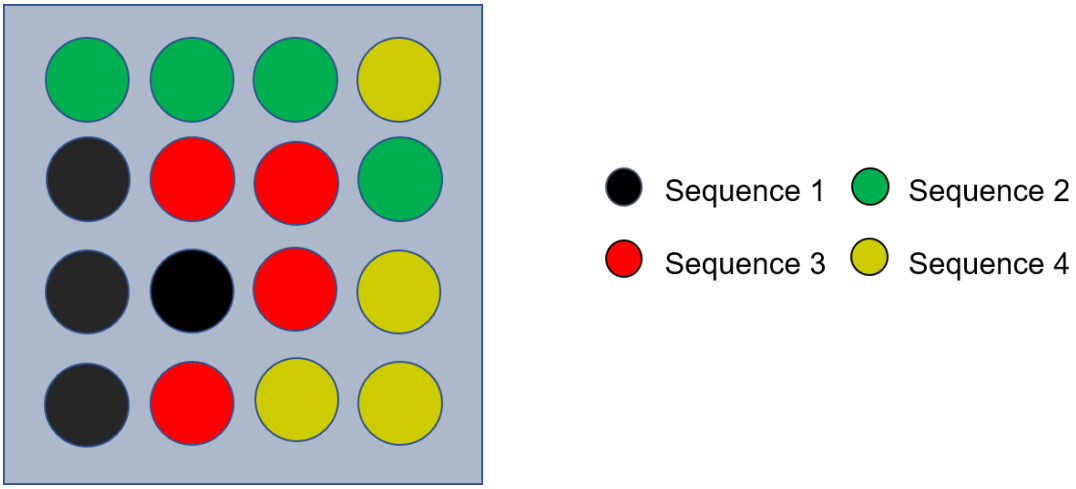

Figure 2.1 DNA sequence arrangement to determine simultaneous orthogonality between DNA library.

2.3 Results and Discussion

2.3.1 Sequence Selection

The library of sequences is shown in Table 2.1. GC content for DNAs was varied between the strands to account for binding strength and to assist in spatial selectivity; G and C base pair incorporation was varied from 0 to approximately 50% of the total sequence. The library was created by individually adding viable sequences to an existing pool that was systematically cross-checked for any partially hybridization or non-specific adsorption to non-complementary DNAs.

Table 2.1. Orthogonal DNA sequences with complements

DNA surface probe (5'-3')	Complementary sequence (5'-3')
1) TTC GAA AGA CTA CGG TAC ATT AAG GAT AAC	GTT ATC CTT AAT GTA CCG TAG TCT TTC GAA
2) TTC GGT TCG TGC TTA TGT GTC TGG ATT TCG	CGA AAT CCA GAC ACA TAA GCA CGA ACC GAA
3) TCT GTG ATT AGC GAT TGT TTA GGT GTA TGC	GCA TAC ACCATAA ACA ATC GCT AAT CAC AGA
4) AAA ATA AAA TAA ATA ATA AAT AAA ATA AAA	TTT TAT TTT ATT TAT TAT TTA TTT TAT TTT

Figure 2.2 demonstrated the total collection of viable orthogonal DNAs manufactured. For each experiment, a single complementary DNA sequence was exposed to all four immobilized DNAs to test for non-specific adsorption. In each instance, the cDNA concentration was 50 nM and was given approximately 15 min including buffer washing to equilibrate to the surface. The signal average taken for SPRI elements that had the same attached DNA probe for non-specific hybridization analysis. For each set, only the interaction between complementary DNA yielded a net increase in Δ%R signal of approximately 0.8%. In comparison, non-complementary, control elements remained relatively stable, and any net signal decrease from the baseline is attributed to the averaging between four different elements. This preliminary data set demonstrates a viable library of orthogonal DNA probes that are selective enough to hybridize its complementary sequence only.

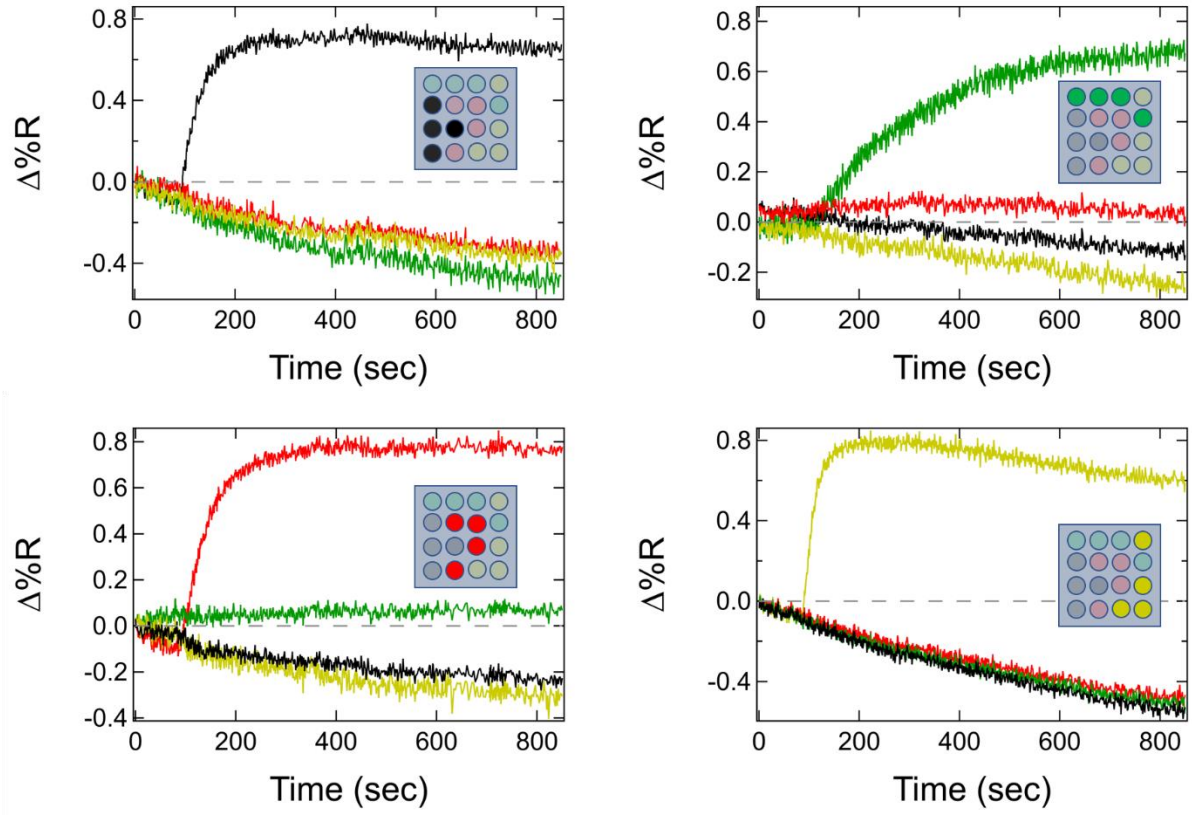

Figure 2.2: Normalized real-time kinetics curve using in complied DNA library. All four selected DNA sequences within library was chemically immobilized on an SPRI imager chip. Then, by running in parallel, each chip was exposed to a single complementary DNA sequences to check for cross hybridization between its single complement, and three non-complementary oligonucleotides. A positive change in Δ%R was only observed between DNA and its complement. All samples were exposed to a 50 nM solution of cDNA.

2.3.2 Real-time Kinetics

Upon confirmation that the DNA library is selective to just its complementary sequence, binding coefficients were determined for all four sequences. For the purposes of discussion, the data displayed and calculated belong solely to sequence 3, but the same analysis was performed for all four. Figure 2.3 demonstrates the binding curve of DNA hybridization versus time, from 10 to 300 nM cDNA concentration. As expected, with the increase in cDNA, a larger Δ%R intensity was observed, with max Δ%R occurring at 300 nM. To quantitate the binding coefficients for duplex formation, each kinetic curve was then fit with the equation

$$(1)\ \Delta\%R(t) = \Delta\%R_{max}\,\theta\,(1 - e^{-\gamma t})$$

Where $\Delta\%R(t)$ is the change in reflectivity due to surface adsorption as a function of time, $\Delta\%R_{max}$ is the maximum change in SPR signal at each concentration, θ is the fraction of total surface coverage, and

$$(2)\ \gamma = k_a C + k_d$$

is the linear relation equation used to find the adsorption and desorption rate constants of DNA hybridization interaction.[10] Figure 2.4 plots the γ values for each concentration measured. Values of k_a and k_d are determined from the slope and y-intercept, respectively, as the linear plot of versus concentration. When taking the ratio between the two, the equilibrium adoption coefficient, K_{Ads}, is found, and represents the binding affinity between probe and analyte. The fitted curves Figure 2.3 closely mirror that of the actual data. When determining the K_{Ads} value for this particular DNA interaction, the equilibrium adsorption constant was $2.1\ (\pm 0.59) \times 10^7\ M^{-1}$, which is what is expected typically for a 30mer base pair DNAs. The summary data for all four sequences is reported in Table 2.2 for k_a, k_d, and K_{Ads} values.

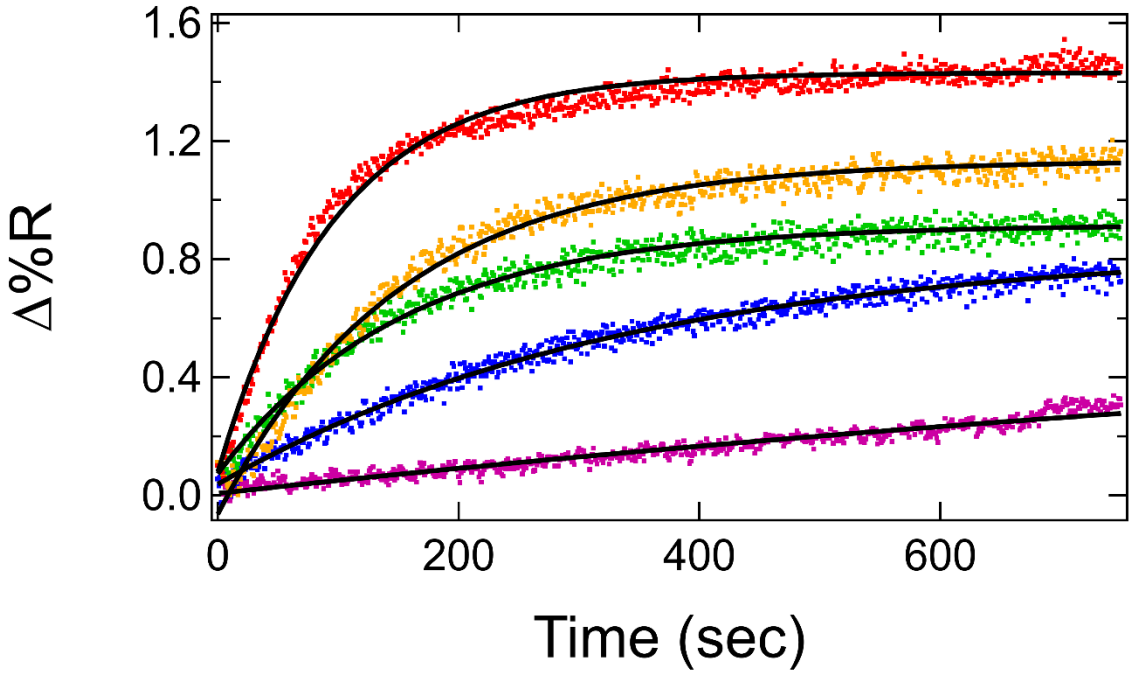

Figure 2.3 Compiled real-time kinetics representative data for the adsorption of cDNA to immobilized probe DNA. Experiments were performed over a range of concentrations and fitted with Equation 1 to yield adsorption kinetic values.

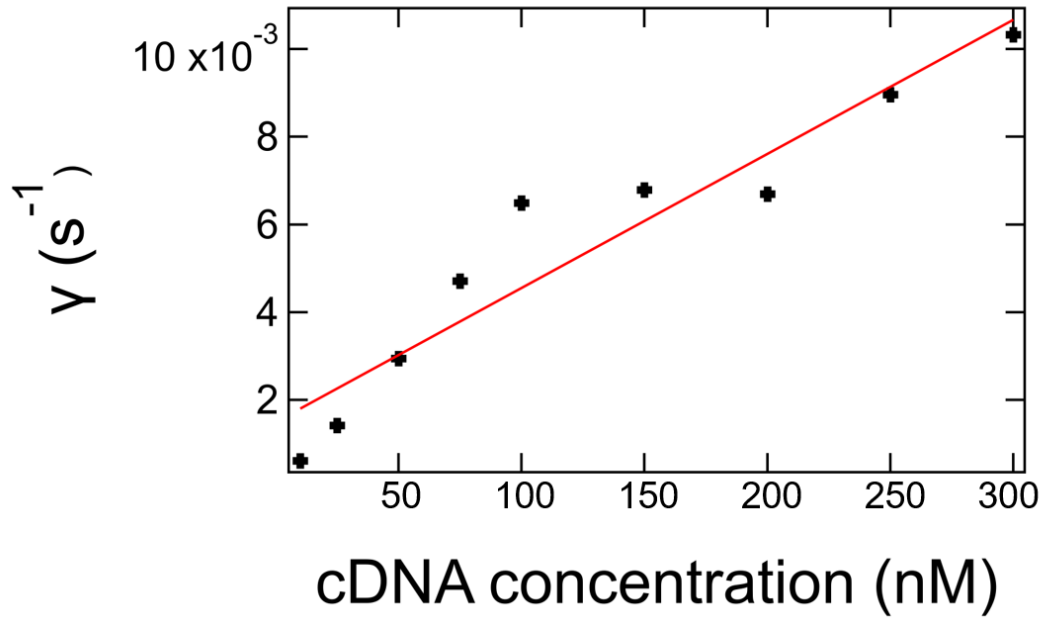

Figure 2.4: Plot of γ values, obtained from cDNA adsorption curves in Figure 2.3, as a function of cDNA concentration. The linear slope corresponds to the adsorption rate constant, k_a, with a value of 3.1 (±0.37) × 10^4 M^{-1} s^{-1}, and the y-intercept corresponds to a desorption rate constant, k_d, determined to be 1.5 (±0.60) × 10^{-3} s^{-1}.

2.3.4 Langmuir Isotherm calculations

An alternative method of evaluating K_{Ads} is to plot the fraction surface coverage θ as a function of cDNA. Assuming the probe monolayer is uniform and DNA surface hybridization is independent from neighboring DNAs, the data can be fit with a Langmuir adsorption isotherm, as shown in Figure 2.5. The maximum change in reflectivity Δ%R (□) was plotted at each measured concentration along with the θ values (●) found using equation 1. When fit with the Langmuir isotherm, the K_{Ads} value was shown to be 2.24 (±0.13) × 10^7 M^{-1}, which is close to the value found using real-time kinetics measurements. Table 2.2 has all measured K_{Ads} from Langmuir isotherm fittings, with all but sequence 1 having K_{Ads} values falling within the calculated error values.

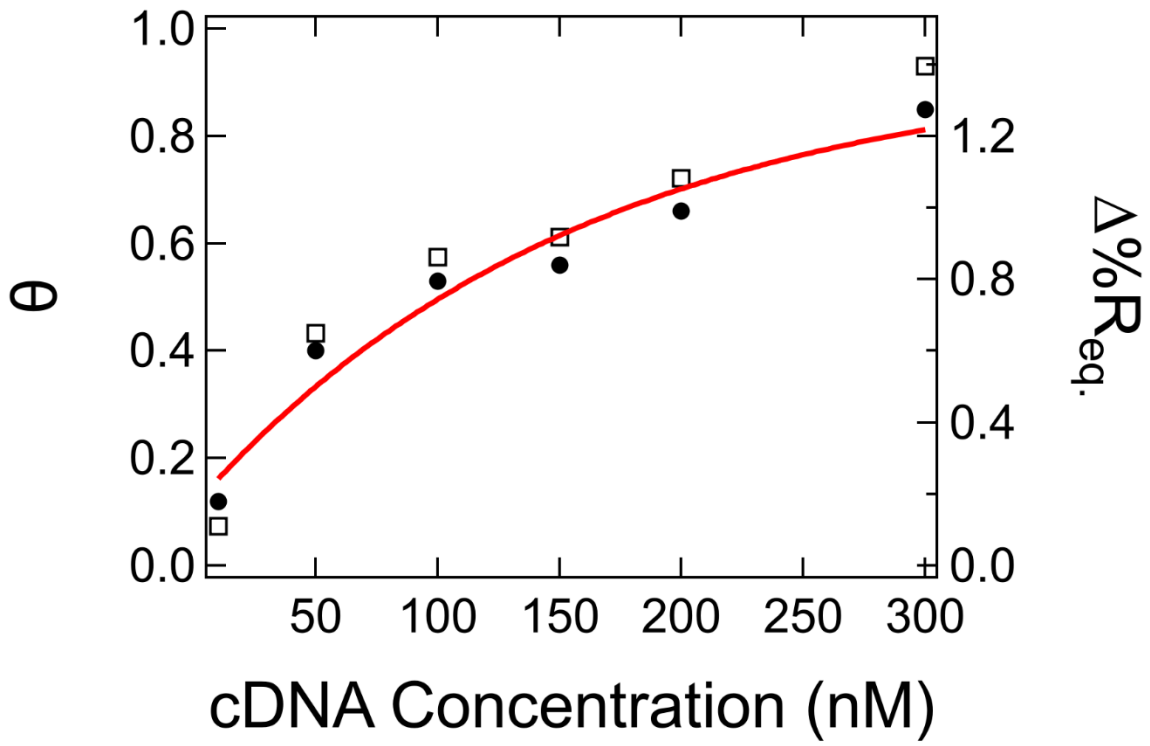

Figure 2.5: Langmuir isotherm fit of equilibrium and kinetic measurements of cDNA adsorption onto DNA probe elements. Equilibrium measurements were performed by introducing complementary DNA to the array surface and measuring Δ%R after 10 min, for each concentration. The maximum signal for the kinetics component was determined from the fit of the adsorption curves, as demonstrated in Figure 2.3. The date for equilibrium (●) and kinetic measurements (□) are plotted as function of concentration. The adsorption constant K_{Ads} was determined to be approximately 2×10^7 M^{-1} by both methods for this DNA hybridization interaction.

Table 2.2. Constants for DNA hybridization Derived by Adsorption Kinetics or Langmuir Isotherm

	ADSORPTION KINETICS			ISOTHERM
SEQUENCE	k_a (M^{-1} s^{-1})	k_d (s^{-1})	K_{Ads} (M^{-1})	K_{Ads} (M^{-1})
1	1.9(±0.18) x 10^4	4.1(±2.2) x 10^{-4}	4.6(±2.1) x 10^7	1.60(±0.41) x 10^7
2	3.2(±0.79) x 10^4	1.6(±0.01) x 10^{-3}	2.0(±1.1) x 10^7	1.75(±0.52) x 10^7
3	3.1(±0.37) x 10^4	1.5(±0.60) x 10^{-3}	2.1(±0.59) x 10^7	2.24(±0.13) x 10^7
4	5.1(±0.51) x 10^4	1.4(±0.87) x 10^{-3}	3.6(±1.9) x 10^7	3.20(±0.71) x 10^7

2.4 Conclusion

In this chapter, a collection of DNA sequences was fabricated and analyzed using real-time SPR imaging. The measurements were performed to first determine orthogonality between oligonucleotides to function as potential unique probe tethers for future multiplexed biosensing applications. Then, k_a, k_d, and K_{Ads} values were determined using real-time kinetics and Langmuir isotherm kinetics via SPRI surface adsorption measurements for each DNA pairing. Future work will focus on the implementation of these sequences as DNA probes for inorganic and metallic nanoparticle signaling.

2.5 Acknowledgements

This work was supported by the National Institutes of Health through grant R01-GM059622.

2.6 References

1. Fasoli, J. B.; Corn, R. M., Surface Enzyme Chemistries for Ultrasensitive Microarray Biosensing with SPR Imaging. *Langmuir* **2015,** *31* (35), 9527-9536.

2. Abbas, A.; Linman, M. J.; Cheng, Q. A., New trends in instrumental design for surface plasmon resonance-based biosensors. *Biosens. Bioelectron* **2011,** *26* (5), 1815-1824.

3. Spoto, G.; Minunni, M., Surface Plasmon Resonance Imaging: What Next? *J. Phys. Chem. Lett.* **2012,** *3* (18), 2682-91.

4. Wong, C. L.; Ho, H. P.; Suen, Y. K.; Kong, S. K.; Chen, Q. L.; Yuan, W.; Wu, S. Y., Real-time protein biosensor arrays based on surface plasmon resonance differential phase imaging. *Biosens. Bioelectron* **2008,** *24* (4), 606-612.

5. Lee, H. J.; Wark, A. W.; Corn, R. M., Creating advanced multifunctional biosensors with surface enzymatic transformations. *Langmuir* **2006,** *22* (12), 5241-5250.

6. Cohen, L.; Walt, D. R., Single-Molecule Arrays for Protein and Nucleic Acid Analysis. *Annu. Rev. Anal. Chem.* **2017,** *10* (1), 345-363.

7. Li, Y.; Lee, H. J.; Corn, R. M., Detection of Protein Biomarkers Using RNA Aptamer Microarrays and Enzymatically Amplified Surface Plasmon Resonance Imaging. *Anal. Chem.* **2007,** *79* (3), 1082-1088.

8. Sendroiu, I. E.; Gifford, L. K.; Luptak, A.; Corn, R. M., Ultrasensitive DNA Microarray Biosensing via in Situ RNA Transcription-Based Amplification and Nanoparticle-Enhanced SPR Imaging. *J. Am. Chem. Soc.* **2011,** *133* (12), 4271-4273.

9. Carrascosa, L. G.; Huertas, C. S.; Lechuga, L. M., Prospects of optical biosensors for emerging label-free RNA analysis. *TrAC, Trends Anal. Chem.* **2016,** *80*, 177-189.

10. Wegner, G. J.; Wark, A. W.; Lee, H. J.; Codner, E.; Saeki, T.; Fang, S. P.; Corn, R. M., Real-time surface plasmon resonance imaging measurements for the multiplexed determination of protein adsorption/desorption kinetics and surface enzymatic reactions on peptide microarrays. *Anal. Chem.* **2004,** *76* (19), 5677-5684.

11. Lee, H. J.; Wark, A. W.; Goodrich, T. T.; Fang, S. P.; Corn, R. M., Surface enzyme kinetics for biopolymer microarrays: a combination of Langmuir and Michaelis-Menten concepts. *Langmuir* **2005,** *21* (9), 4050-4057.

12. Gurkov, T. D., Adsorption kinetics under the influence of barriers at the subsurface layer. *Colloid Polym. Sci* **2011,** *289* (17), 1905-1915.

13. Bourdillon, C.; Demaille, C.; Moiroux, J.; Savéant, J.-M., Activation and Diffusion in the Kinetics of Adsorption and Molecular Recognition on Surfaces. Enzyme-Amplified

Electrochemical Approach to Biorecognition Dynamics Illustrated by the Binding of Antibodies to Immobilized Antigens. *J. Am. Chem. Soc.* **1999,** *121* (11), 2401-2408.

14. Chen, Y. L.; Nguyen, A.; Niu, L. F.; Corn, R. M., Fabrication of DNA Microarrays with Poly(L-glutamic acid) Monolayers on Gold Substrates for SPR Imaging Measurements. *Langmuir* **2009,** *25* (9), 5054-5060.

15. Sendroiu, I. E.; Corn, R. M., Nanoparticle diffraction gratings for DNA detection on photopatterned glass substrates. *Biointerphases* **2008,** *3* (3), FD23-FD29.

16. Zhou, W. J.; Chen, Y. L.; Corn, R. M., Ultrasensitive Microarray Detection of Short RNA Sequences with Enzymatically Modified Nanoparticles and Surface Plasmon Resonance Imaging Measurements. *Analytical Chemistry* **2011,** *83* (10), 3897-3902.

17. Chen, Y.; Nakamoto, K.; Niwa, O.; Corn, R. M., On-chip synthesis of RNA aptamer microarrays for multiplexed protein biosensing with SPR imaging measurements. *Langmuir* **2012,** *28* (22), 8281-8285.

18. Fang, S. P.; Lee, H. J.; Wark, A. W.; Corn, R. M., Attomole microarray detection of MicroRNAs by nanoparticle-amplified SPR imaging measurements of surface polyadenylation reactions. *J. Am. Chem. Soc.* **2006,** *128* (43), 14044-14046.

19. Xu, F.; Dong, H.; Cao, Y.; Lu, H.; Meng, X.; Dai, W.; Zhang, X.; Al-Ghanim, K. A.; Mahboob, S., Ultrasensitive and Multiple Disease-Related MicroRNA Detection Based on Tetrahedral DNA Nanostructures and Duplex-Specific Nuclease-Assisted Signal Amplification. *ACS Appl. Mater. Interfaces* **2016,** *8* (49), 33499-33505.

20. Nam, J.-M.; Thaxton, C. S.; Mirkin, C. A., Nanoparticle-Based Bio-Bar Codes for the Ultrasensitive Detection of Proteins. *Science* **2003,** *301* (5641), 1884.

21. Smith, E. A.; Corn, R. M., Surface plasmon resonance imaging as a tool to monitor biomolecular interactions in an array based format. *Appl. Spectrosc.* **2003,** *57* (11), 320A-332A.

22. Couture, M.; Zhao, S. S.; Masson, J. F., Modern surface plasmon resonance for bioanalytics and biophysics. *Phys. Chem. Chem. Phys* **2013,** *15* (27), 11190-11216.

Chapter 3

Characterizing the Incorporation of DNA into Single NIPAm Hydrogel Nanoparticles with Surface Plasmon Resonance Imaging Measurements

3.1 Introduction

A variety of polymeric hydrogel nanoparticles (HNPs) are currently employed as nanoscale materials for the uptake, transport, collection, and release of various therapeutics and biomarkers, including drug molecules, peptides, proteins, nucleic acids, antibodies, and even small metallic nanoparticles.[1-10] For example, *N*-isopropylacrylamide (NIPAm)-based hydrogel nanoparticles that incorporate various ratios of *tert*-butyl and acrylic acid (AAc) have been optimized for the specific uptake and delivery of the polypeptide melittin, the active component in honey bee venom,[11] and the toxins in elapid snake venom.[12] NIPAm-based HNPs have also been engineered to incorporate bioaffinity binding sites,[13] such as mannose sugars for the specific uptake of lectins.[14]

To further explore the loading capabilities of hydrogel nanoparticles, we synthesize 230 nm NIPAm-based nanoparticles that incorporate single-stranded DNA (ssDNA) directly into the polymer, forming DNA–HNPs, and then quantitate their ssDNA binding affinity and exonuclease activity through a combination of single nanoparticle surface plasmon resonance imaging (SPRI) microscopy, fluorescence measurements, dynamic light scattering (DLS), and transmission electron microscopy (TEM). The incorporation of ssDNA is an obvious choice as a versatile binding site due to its ability to hybridize to complementary nucleic acid sequences with excellent specificity,[15] to be hydrolyzed[16] or ligated[17] with various high-efficiency DNA enzymes, and to fold into configurations that either bind molecular targets or exhibit enzymatic reactivity, releasing potential cargo.[18-20] NIPAm-based hydrogels that incorporate and release ssDNA using these mechanisms have been used extensively in a thin film format, primarily on planar surfaces, but also in a core-shell nanoparticle format.[4, 21-23] For example, DNA–HNPs were used in the uptake, delivery, and release of small interfering RNA to infected cells.[9, 24-25]

Figure 1 incorporates a mixture of acrylamide-modified species in ratios similar to those used in our previous work[14] but with the addition of acrylic phosphoramidite-modified 30mer ssDNA. Acrylamide has demonstrated reactivity toward DNA, most notably via a Michael addition reaction with guanine, cytosine, and adenosine nucleotides.[26-27] These types of Michael addition reactions cause acrylamide to form DNA adducts, which have shown to affect the biological activity of regulatory systems.[28-30] In the case of DNA–HNP formations, this interaction could give rise to additional polymerization sites, aiding in the incorporation of DNA as a whole.[30] We theorize that this additional acrylamide cross-linking accounts for only observing approximately 35% of the incorporated ssDNA being available for hybridization with complementary ssDNA or enzymatic exonuclease activity.

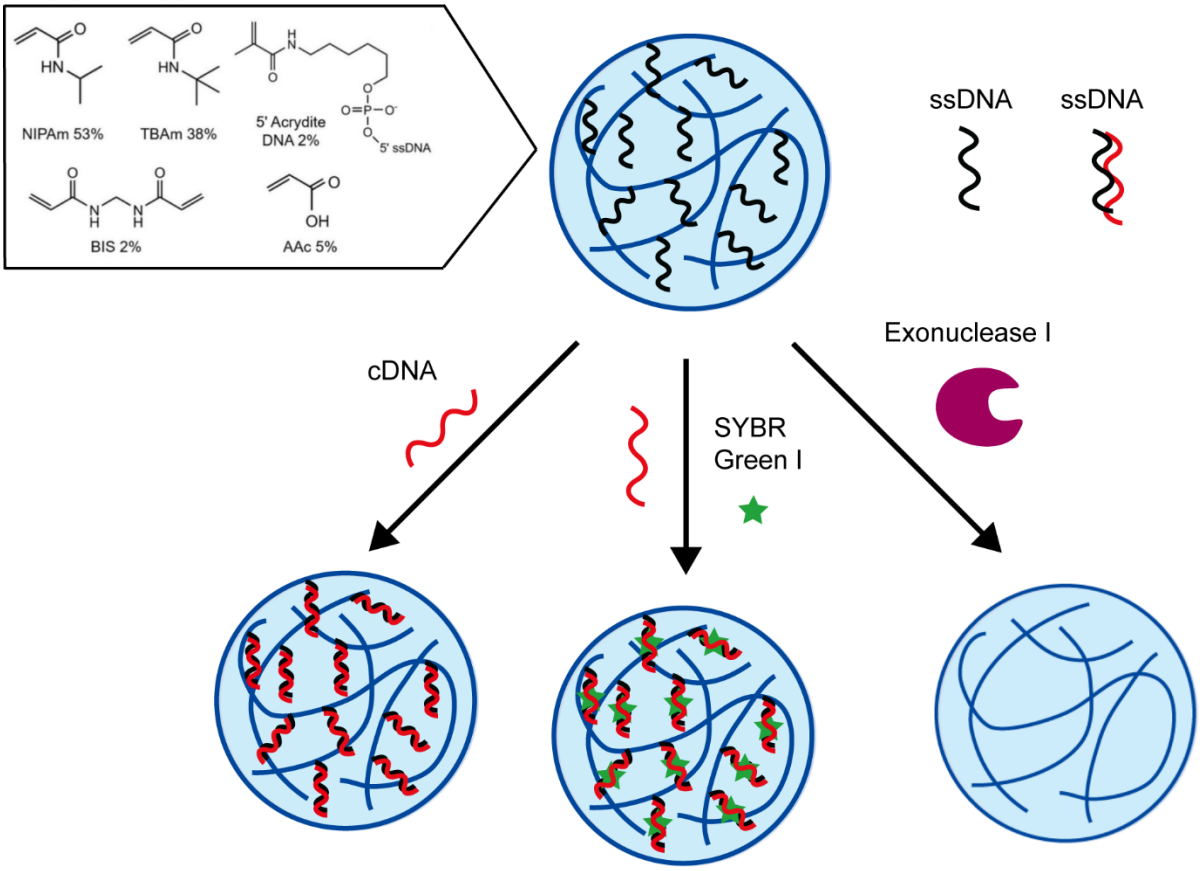

Figure 3.1. DNA-incorporated hydrogel nanoparticles (HNPs) were composed of *N*-isopropylacrylamide (NIPAm, 53 mol %), *N*-*tert*-butylacrylamide (TBAm, 38 mol %), acrylic acid (AAc, 5 mol %), *N*,*N*'-methylenebis(acrylamide) (BIS, 2 mol %), and 5'-modified acrylic phosphoramidite DNA (2 mol %). Following purification, incorporated DNA was tested to demonstrate accessibility and chemical activity, via specific complementary sequence hybridization to form double stranded DNA (dsDNA), fluorescent dyeing, and enzymatic activity through DNA hydrolysis.

3.2 Methods

3.2.1 Hydrogel Nanoparticle Materials

N-Isopropylacrylamide (NIPAm), acrylic acid (AAc), sodium dodecyl sulfate (SDS), and ammonium persulfate (APS) were obtained from Sigma-Aldrich, Inc. (St. Louis, MO). *N*,*N*-Methylenebis(acrylamide) (BIS) was obtained from Fluka (St. Louis, MO). *N*-*tert*-Butylacrylamide (TBAm) was obtained from Acros Organics (Geel, Belgium). All DNAs were

purchased from Integrated DNA Technologies (Coralville, IA). NIPAm was recrystallized from hexane before use. All other chemicals were used as received.

3.2.2 Hydrogel Nanoparticle Synthesis

HNP synthesis was adapted from the procedure detailed in *Cho, et. al.*[11] The monomers NIPAm (53 mol %), TBAm (38 mol %), AAc (5 mol %), and BIS (2 mol %) were dissolved in 1.7 mL of nanopure water in a round-bottom flask for a total monomer concentration of 21 mM. TBAm was dissolved in 50 μL of ethanol before addition to the monomer solution. The surfactant SDS (0.25 mg) was also added to the monomer solution to control the nanoparticle size. Nitrogen gas was bubbled through the solution for 30 min. Following the addition of a 100 μL aqueous solution containing 1 mg of APS, the polymerization reaction was carried out in an oil bath preset to 60 °C. After 30 min of reaction time, 1.3 μmol (1 mM aqueous solution) of DNA was added to the reaction flask via syringe, and the polymerization reaction was allowed to proceed for an additional 2.5 h under a nitrogen atmosphere. The resulting solution was purified by dialysis using a 12–14 kDa molecular weight cut off dialysis membrane against an excess amount of nanopure water (changed three times a day) for 3 days. Hydrogel nanoparticle size distribution and concentration were measured in aqueous solutions at 25 °C on a dynamic light scattering (DLS) instrument equipped with Zetasizer software (Zetasizer Nano ZS, Malvern Instruments Ltd., Worcestershire, U.K.) and NanoSight NS300 nanoparticle tracking and analysis microscopy system (Malvern Panalytical). Cryo-TEM images were obtained using 3μL of sample solution applied on a glow-discharged Quantifoil grid (Quantifoild, R2/2) and then loaded on a Leica EMGP plunger (Leica Biosystem). The grid was quickly plunged into liquid propane after blotting away the excess liquid, and the hydrogel particles were then embedded in a thin layer of vitrified ice on the grid. The cryo-grid was then transferred into a JEM-2100F

electron microscope using a Gatan cryo-transfer holder (Gatan, Inc.). The electron microscope was operated at 200 kV with a field emission gun, and the specimen was examined under minimum dose system. The images were recorded on a OneView camera (Gatan, Inc.) at 40000× magnification, corresponding to 0.28nm per pixel at specimen space.

3.2.3 Substrate Preparation

The Au substrates were coated by the thermal vapor deposition of a 1 nm Cr adhesion layer and 45 nm Au onto borosilicate No. 1.5 coverslips (Fisherbrand, Pittsburgh, PA). The Au surface was immobilized with 1-undecanethiol (C11) by immersing the Au substrate into a 1 mM C11/EtOH solution. The Au surface was partitioned using adhesive silicon isolation wells (Electron Microscopy Sciences, Hatfield, PA).

3.2.4 SPRI Microscopy Measurements

The SPRI microscope setup is described in a previous publication.[31] The microscope was built into the frame of an IX51 inverted microscope (Olympus, Tokyo, Japan). A 1 mW, 814 nm diode laser (Melles Griot, Carlsbad, CA) was expanded and collimated using a spatial filter (Newport Corp., Newport Beach, CA). The beam was polarized and focused with a lens (f= 200 mm) and then directed onto the back focal plane of a 100× 1.49 high numerical aperture objective (Olympus). The beam was directed upward near the edge of the objective by a gold-coated knife-edge mirror (Thorlabs, Newton, NJ). The reflected image was passed out the other side of the objective and acquired by an Andor Neo sCMOS camera (South Windsor, CT). Each 3 s reflectivity image was acquired by accumulating 30, 11-bit, 0.1 s exposures.

3.2.5 Enzymatic SPRI Measurements

Exonuclease I (5 μL of 20 U/μL; New England Biolabs) was added to 1–10 diluted 10× reaction buffer (67 mM glycine-KOH, 6.7 mM $MgCl_2$, 10 mM β-ME, pH 9.5) and a 1–10 stock-

diluted D1-HNP solution to a final volume of 500 μL in nanopure water. The solution was incubated at 37 °C for 1 h before carrying out three wash cycles similar to the fluorescence measurements described above. After the final wash, the solution was then resuspended to a final volume of 50 μL.

3.3 Results and Discussion

3.3.1 Synthesis and Characterization of DNA–HNPs

Four types of DNA–HNPs were synthesized and then characterized via a combination of DLS, TEM imaging, fluorescence measurements and single-nanoparticle surface plasmon resonance imaging (SPRI) microscopy. DNA–HNP size distribution was obtained by DLS and confirmed using TEM imaging. Through the combination of fluorescence loss measurements and nanoparticle tracking measurements, an incorporated DNA concentration of approximately 22 000 ± 1,000 fluorophores per nanoparticle was found.

The primary DNA sequence used for DNA–HNPs analysis is denoted D1; its complementary sequence is labeled D1c and control sequence D1nc. To analyze potential influences of the nucleotides used the during synthesis, three additional sequences were also used: a modified 30mer sequence from Lilienthal, et. al.,[18] a poly-T sequence, and a poly-A sequence, denoted D2, D3, and D4 respectively. All sequence used are summarized in Table 1. A large amount of D1 ssDNA was found incorporated into the HNPs, suggesting some degree of cooperativity between the ssDNA and the acrylamide polymerization process. SPRI nanoparticle measurements showed that the resultant DNA–HNPs were able to specifically hybridize complementary 30mer ssDNA (D1c) with nanomolar binding efficiency and were easily hydrolyzed by the DNA enzyme exonuclease I.

Table 3.1. ssDNA sequences incorporated into various batches of DNA–HNPs

label	DNA sequence
D1	5'-acrydite- TCT GTG ATT AGC GAT TGT TTA GGT GTA TGC-3'
D1c	5'-GCA TAC ACC TAA ACA ATC GCT AAT CAC AGA-3'
D1nc	5'-CGA AAT CCA GAC ACA TAA GCA CGA ACC GAA-3'
D2	5'-acrydite- TTT TTT TTT TTT TTT TTT TCT TCA TTG TTT-3'
D3	5'-acrydite-TTT TTT TTT TTT TTT TTT TTT TTT TTT TTT-3'
D4	5'-acrydite-AAA AAA AAA AAA AAA AAA AAA AAA AAA AAA-3'

The primary method used to characterize the activity of the DNA–HNPs was near-infrared single-nanoparticle SPRI microscopy. This relatively new microscopic single-nanoparticle method has been employed recently to detect and characterize distributions of polymeric, oxide, and metal nanoparticles based on the nanoparticle's integrated refractive index.[32-35] In a single-nanoparticle SPRI measurement, a total internal reflection microscope geometry is used with an 814 nm laser to excite traveling wave surface plasmon polaritons (SPPs) onto a 45 nm gold thin film attached to a microscope slide cover. Upon exposure to an aqueous solution of nanoparticles, SPRI reflectivity images (100 μm x 100 μm) are obtained every 3 s from this microscope for 10 min. These images are subtracted sequentially from each other to create a set of 200 SPRI differential reflectivity (Δ% R) images.

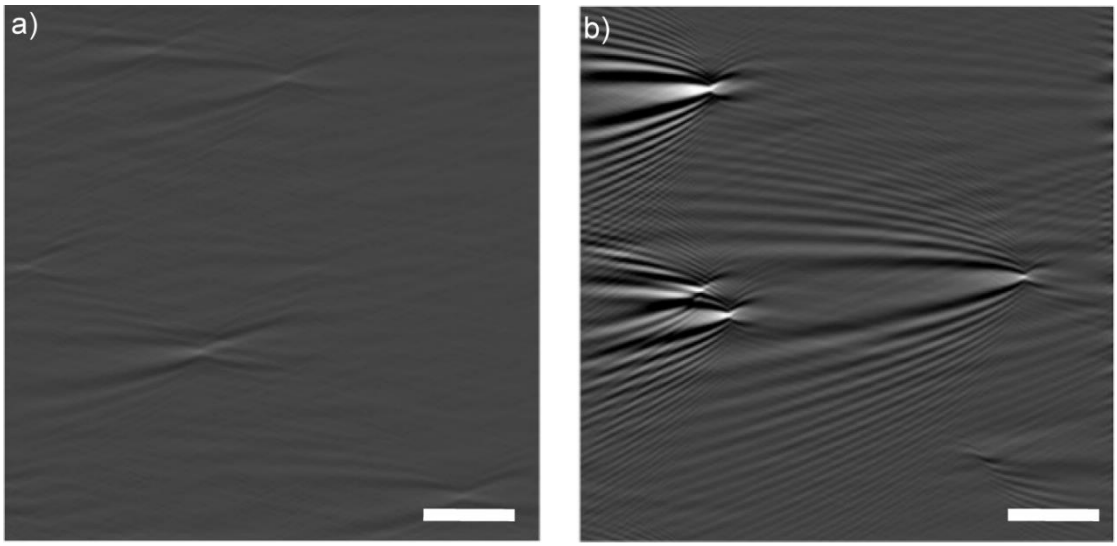

Figure 3.2. Example SPRI differential reflectivity images of (a) HNPs and (b) DNA-HNPs, irreversibly adsorbing to the gold thin-film surface. The scale bar for both images is 10 μm.

Two examples of these 3 s SPRI differential reflectivity images obtained during the exposure of a gold thin film to solutions of HNPs and DNA–HNPs are shown in Figure 2. The gold has been modified with a 1-undecanethiol monolayer to create a hydrophobic surface onto which both nanoparticles irreversibly adsorb through hydrophobic forces. Each irreversible nanoparticle binding event on the gold surface in the 3 s time window creates a distinctive point diffraction pattern in the image due to the interaction of the nanoparticle refractive index with the traveling SPPs. The shape and intensity of these diffraction patterns have been modeled and quantitated previously;[31-32] the intensity of each DNA–HNP binding event can be quantitated to obtain a single-nanoparticle reflectivity change value, $\Delta\% R_{NP}$. We have shown in previous papers that $\Delta\% R_{NP}$ depends on both the size and composition of the adsorbed nanoparticle. As such, $\Delta\% R_{NP}$ can be thought of as the "integrated refractive index" of the adsorbed nanoparticle. A collection of 300–400 $\Delta\% R_{NP}$ values for synthesized DNA–HNPs was obtained over several experiments, and results are summarized in Table 2 along with DLS size distribution measurements.

Table 3.2. Hydrodynamic Size Measurements from DLS for Hydrogel Nanoparticles and Statistics from Single-Nanoparticle SPRI measurements for Hydrogel Nanoparticles

nanoparticle	diameter (nm)	$<\Delta\%R_{NP}>$	standard deviation (s)	95% CI	# of NPs
D0-HNP	246 ± 3	0.51	0.16	0.02	357
D1-HNP	234 ± 5	5.18	2.04	0.22	320
D2-HNP	202 ± 2	2.38	1.17	0.11	424
D3-HNP	216 ± 1	0.59	0.32	0.32	304
D4-HNP	196 ± 3	2.11	0.98	0.10	403
D1-HNP + Exonuclease I	-	3.16	2.09	0.31	180

Figure 3 plots two data sets of $\Delta\%\ R_{NP}$ values obtained from two different group experiments, one for the adsorption of HNPs without DNA incorporation (D0) and one for the adsorption of D1-HNPs, both as a function of time. The two types of HNPs have significantly different average $\Delta\%\ R_{NP}$ values (which we denote as $<\Delta\%R_{NP}>$) of 0.51 ± 0.02% for D0-HNPs and 5.18 ± 0.22% for D1-HNPs, with ranges represented as 95% confidence intervals. The addition of acrylamide-modified ssDNA to the NIPAm polymerization has led to an almost 10-fold increase in $<\Delta\%\ R_{NP}>$. In contrast, DLS measurements on the two types of nanoparticles show only a slight change in nanoparticle diameter from 246 ± 3 nm to 234 ± 5 nm for D0-HNPs and D1-HNPs respectively. Cryo-TEM images of D1–HNPs were collected also to show that the particles are not aggregating together and to further corroborate their sizes, as demonstrated in Figure 4.

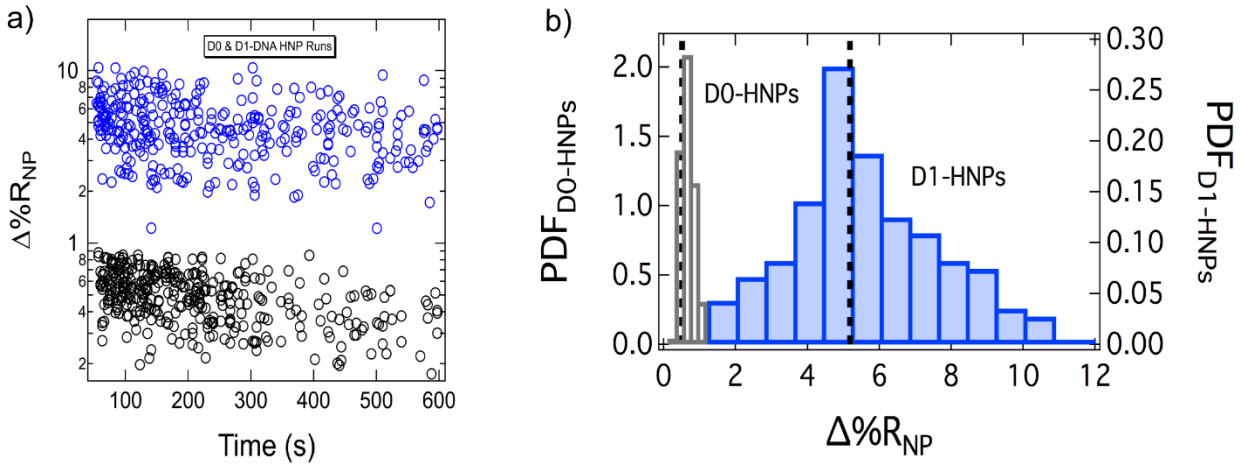

Figure 3.3. (a) Time-dependent distribution of Δ% R_{NP} values of HNPs with (blue) and without (black) DNA incorporation, measured in separate experiments. Each circle represents the Δ% R_{NP} for a single HNP, irreversibly adsorbing to the chemically modified surface. (b) Δ% R_{NP} frequency distribution histograms obtained from the SPRI adsorption measurements of HNPs (transparent gray bars) and DNA–HNPs (blue bars). The averages for each distribution are denoted by the dotted black lines within each distribution. Average Δ% R_{NP} for HNPs and DNA–HNPs are 0.51± 0.02 and 5.18 ± 0.22%, respectively.

The large increase in <Δ% R_{NP} > when comparing D0-HNPs with D1-HNPs is due to an increase in both nanoparticle density and refractive index in the presence of acrylamide-modified ssDNA (Figure 3). This large increase strongly suggests that (i) a significant amount of 30mer ssDNA has been incorporated into the D1-HNP and (ii) the presence of the acrylamide-modified ssDNA during polymerization has altered the structure of the hydrogel in a manner that has increased its density. Surprisingly, the increase is <Δ% R_{NP} > , is significantly less for 30mer sequences that contain more thymine nucleotides: for D2-HNPs, which have over half of the 30mer nucleotide sequence replaced by thymine, the signal drops to 2.38 ± 0.11%, and for D3-HNPs, which incorporate a 30mer poly-T ssDNA, the signal drops all of the way down to 0.59 ± 0.03%, just slightly larger than that for the D0-HNPs. These additional measurements strongly suggest that the large increase in <Δ% R_{NP} > for the DNA–HNPs can be attributed to previously observed Michael addition reactions of the acrylamide with adenine, cytosine, and guanine

nucleotides during the polymerization process.[27, 29, 36] Thymine nucleotides do not react with acrylamide at physiological pH and thus there is no incorporation of the poly-T ssDNA into the D3 HNPs.[27] This is further corroborated by the observed incorporation of 30mer poly-A ssDNA 30mers into the D4 HNPs, where the signal once again increases since adenine is capable of undergoing a Michael addition reaction. The reaction of acrylamide with A, C, and G in the ssDNA greatly assists in the overall incorporation of ssDNA into the nanoparticle and also provides additional cross-linking of the ssDNA and hydrogel. A second potential mechanism for sequence-dependent ssDNAs incorporation would be the formation of self-complementary secondary structures between ssDNA that lead to greater packing and thus denser incorporation of ssDNA into the HNPs. These interactions are typically much weaker, and DNA-folding calculations are shown to have a free energy of -0.98 kcal/mol,[37] proving that the D1 sequence does not show a large degree of folding or secondary structure.

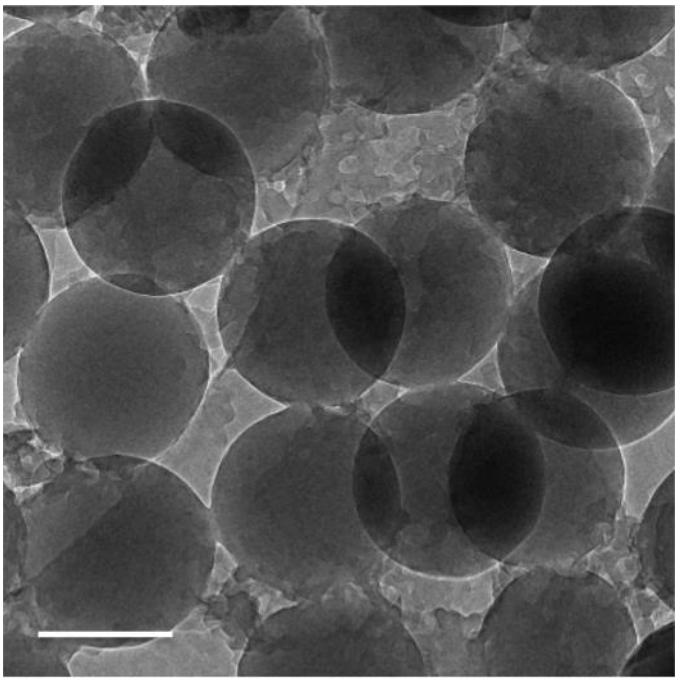

Figure 3.4. Cryo-TEM image of vitrified D1-HNPs. The scale bar is 200 nm.

3.3.2. Hybridization Uptake of Complementary ssDNA by DNA–HNPs

To determine the ability of the DNA–HNPs to uptake and hybridize complementary ssDNA from solution, we employed a combination of fluorescence and single-nanoparticle SPRI measurements. Using D1-HNPs, fluorescence loss measurements were performed using fluorescently labeled complementary DNA (D1c) to estimate the loading capacity of DNA into the HNPs. On average, approximately 20 000 fluorophore-modified ssDNAs were incorporated into the DNA–HNPs. Further details are given in the Supplemental Information.

To verify that the incorporation of complementary D1c into the D1-HNPs was due to hybridization to form dsDNA, fluorescence measurements using the intercalation of SYBR Green I into dsDNA were performed to demonstrate duplex formation in the DNA–HNPs. The fluorescence spectrum of DNA–HNPs with either complementary (solid blue line) or noncomplementary (dotted black line) ssDNA, both at a 10 nM solution, is shown in Figure 5. SYBR Green I preferentially stains dsDNA formations, and, as seen in Figure 5, a strong fluorescence signal was only observed in the presence of complementary ssDNA. These results demonstrate that the uptake of complementary ssDNA into the DNA–HNPs is driven by duplex formation to create dsDNA.

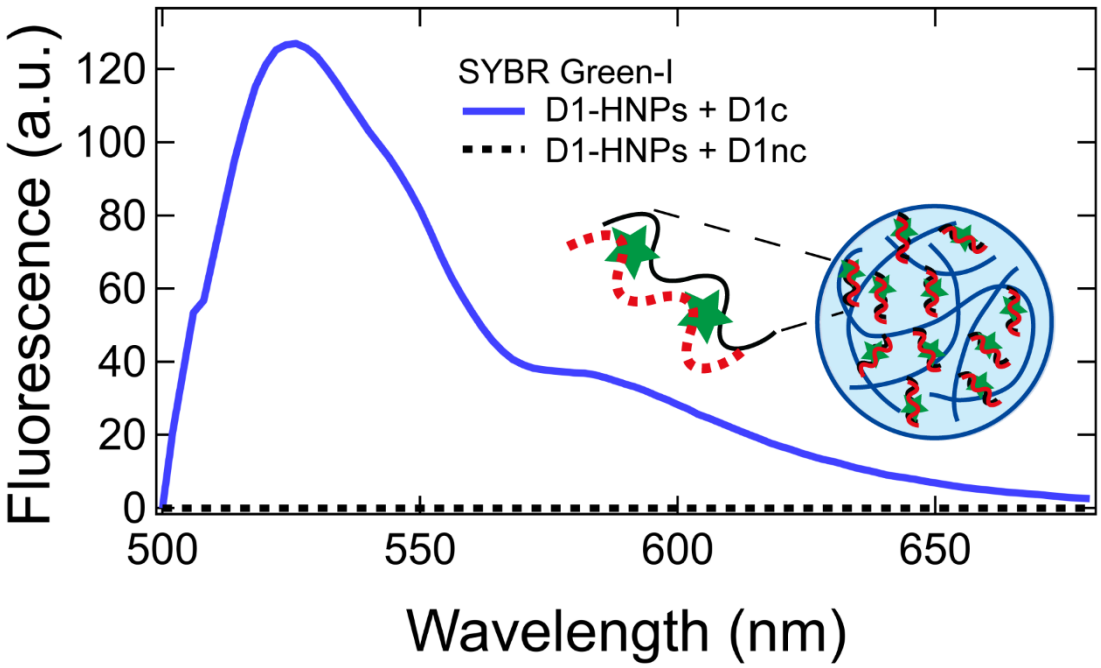

Figure 3.5. Fluorescence spectra of D1-HNPs in the presence of SYBR Green I dye and either complementary (D1c) or noncomplementary (D1nc) ssDNA. D1-HNPs were mixed initially with either of the ssDNA, followed by the fluorescent dye. Parallel measurements were then performed after three centrifuge/wash cycles before D1-HNPs mixtures were resuspended in buffer solution. The solid blue curve indicated the formation of dsDNA within D1-HNPs with its complementary sequence, D1c, and SYBR Green staining. No fluorescence was observed in the D1nc mixture (dotted black line), as SYBR Green preferentially stains dsDNA formations.

Single-nanoparticle SPRI measurements were used to quantitate the hybridization uptake of complementary ssDNA into the D1-HNPs. Figure 6 shows the change in the $\Delta\%\ R_{NP}$ distribution of the DNA–HNPs after exposure to a 100 nM complementary ssDNA solution. The average $<\Delta\%\ R_{NP}>$ increased by approximately 2% (from 5.18 ± 0.22 to 7.11 ± 0.25%). As a control experiment, negligible change in $<\Delta\%R_{NP}>$ was observed for DNA-HNPs in the presence of 100 nM noncomplementary ssDNA. These SPRI measurements confirm the ability of these HNPs to incorporate target ssDNA; however, only a 2% increase in $<\Delta\%R_{NP}>$ suggests

that just 35% of the DNA is accessible for sequence-specific hybridization.

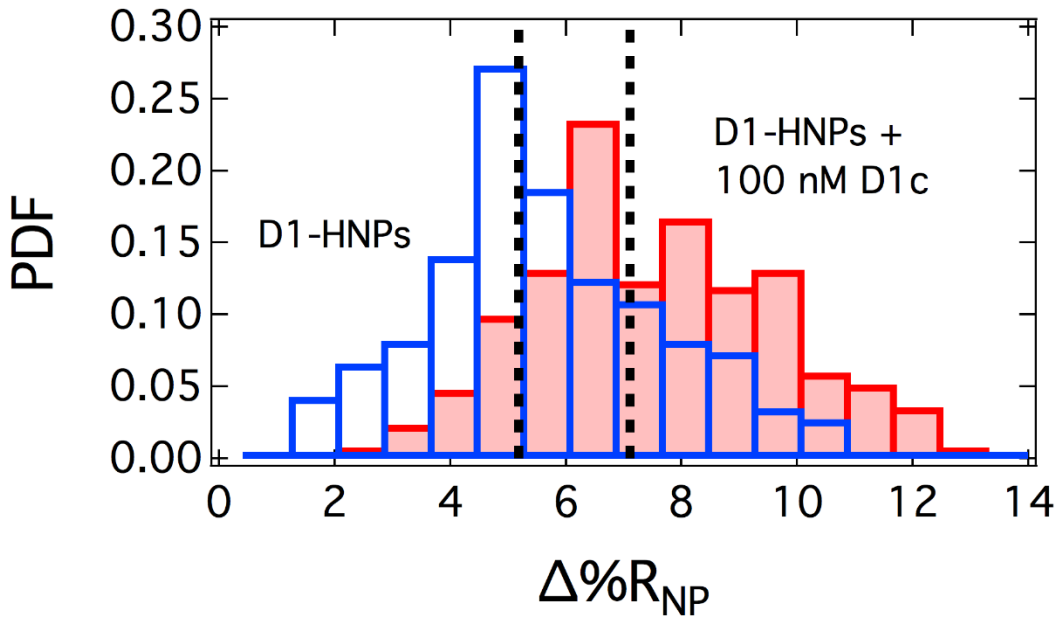

Figure 3.6. Δ% R_{NP} frequency distribution histograms obtained from the SPRI adsorption measurements of D1-HNPs onto Au surfaces. The transparent blue bars indicate D1-HNPs before exposure to its complementary sequence, D1c. When exposed to D1c, D1-HNPs uptake the ssDNA, causing a shift in Δ% R_{NP} signal, shown as solid red bars. The dotted black lines for each distribution denote the averages, 5.18 ± 0.22 and 7.11 ± 0.25% for D1-HNPs and D1-HNPs in the presence of D1c, respectively.

Additional single nanoparticle SPRI measurements were performed to determine the concentration dependence of the hybridization uptake of complementary ssDNA into the DNA–HNPs. The change in the average $<\Delta\% R_{NP}>$ for the DNA–HNPs is plotted against the log of complementary ssDNA concentration in Figure 7. The solid red line in the figure is a fit of this concentration dependence to a Langmuir adsorption isotherm. The Langmuir adsorption coefficient for this fit is 4.89×10^8 M^{-1}; the inverse of this number, about 2 nM, is the concentration for which half of the adsorption sites are filled. The value for the Langmuir adsorption coefficient is approximately 5–10 times higher than that observed for the adsorption of complementary ssDNA to ssDNA monolayers on gold thin films;[31] this result suggests that

duplex formation is more favorable in the DNA–HNPs as compared to that on a surface, most likely due to the increased flexibility and access of the ssDNA in the three-dimensional hydrogel format.

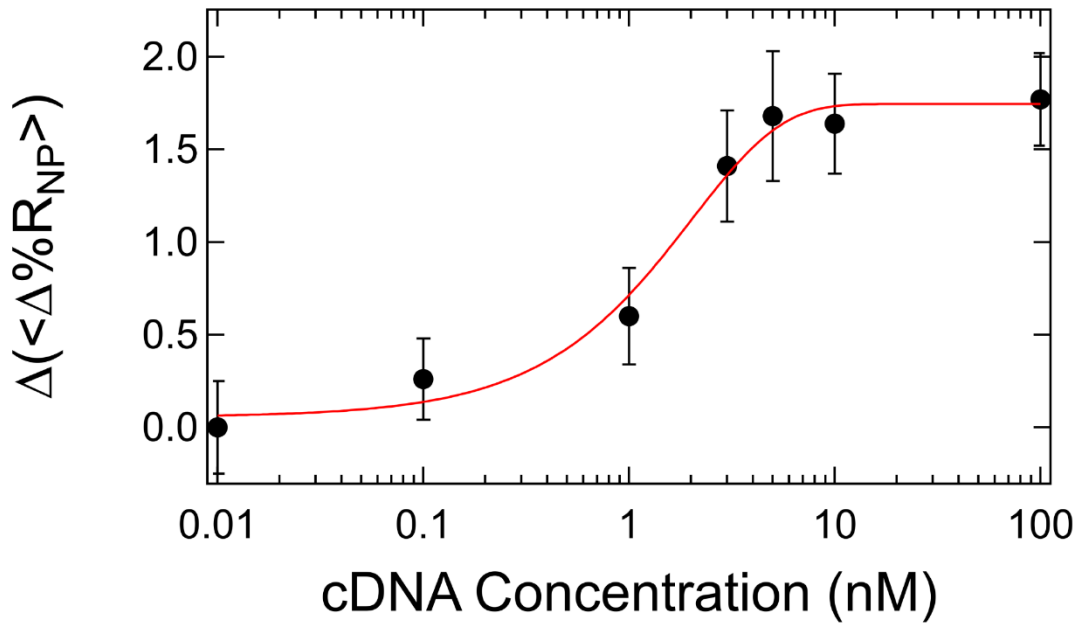

Figure 3.7. Langmuir isotherm fit of the change in < Δ% R_{NP}>, comparing unoccupied D1-HNPs with D1-HNPs loaded with D1c. Each measurement is the difference between the Δ% R_{NP} signal concentration at a D1c concentration and empty D1-HNPs. The adsorption constant K_{ads} was determined to be 4.89 × 10^8 M^{-1}.

3.3.3 Enzymatic Hydrolysis of ssDNA in DNA-HNPs

As a demonstration of the bioavailability of the ssDNA in the HNPs, SPRI measurements were used to monitor the enzymatic hydrolysis of the ssDNA in the nanoparticles. The DNA enzyme exonuclease I will exclusively hydrolyze ssDNA but not dsDNA. SPRI nanoparticle measurements were performed on DNA–HNPs after exposure to a solution of exo I for 1 h; Figure 8 plots Δ% R_{NP} distributions pre-exposure (blue bars) and postexposure (green bars) of exo I. A significant decrease in < Δ% R_{NP}> was observed, dropping the value from 5.18 to 3.16 ± 0.31% after enzymatic activity; we attribute this decrease to the hydrolysis of ssDNA in the DNA–HNP. Interestingly, this decrease in <Δ% R_{NP}> is approximately the same value as the

maximum amount of increase in $<\Delta\%R_{NP}>$ observed in hybridization adsorption experiments in Figure 7, maintaining roughly the same percentage of accessibility as DNA duplex formation.

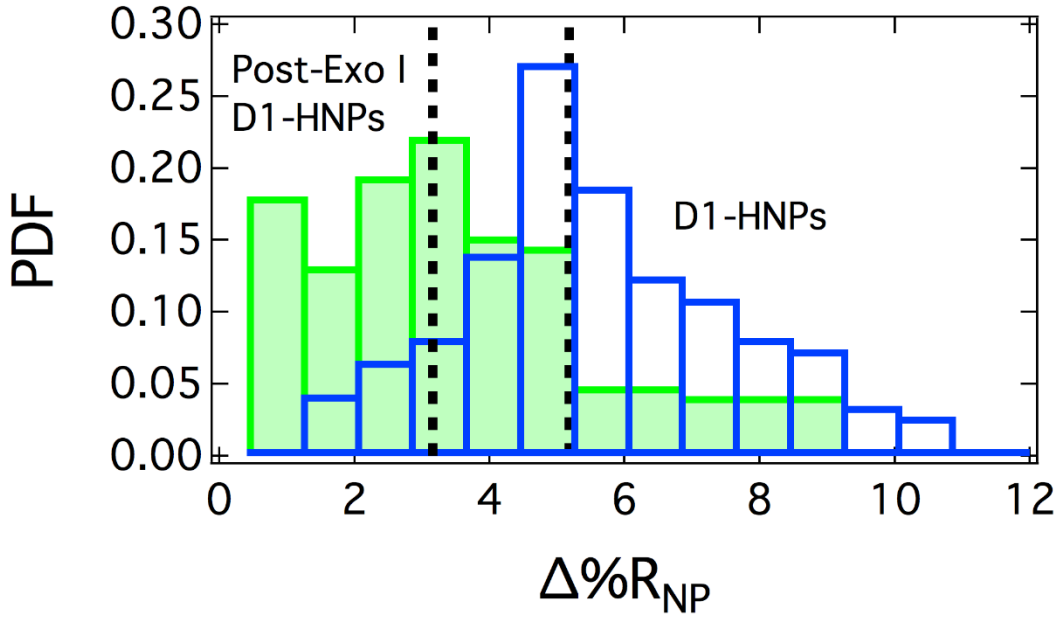

Figure 3.8. Single-nanoparticle SPRI frequency distributions comparing DNA–HNPs distributions before (transparent blue bars) and after (solid green bars) exposure to exonuclease I. The dotted lines for each distribution represent the $\Delta\%$ R_{NP} averages for pre-exposure and postexposure, 5.18 ± 0.22 and 3.16 ± 0.31%, respectively.

3.4 Conclusions

In conclusion, we have shown in this chapter that DNA–HNPs can be prepared via the incorporation of acrylamide-modified 30mer ssDNA and that they can be used to uptake complementary ssDNA by hybridization adsorption/incorporation. Moreover, the ssDNA in the DNA–HNPs can undergo enzymatic hydrolysis, demonstrating the availability of the incorporated ssDNA to enzymatic activity. An almost 10-fold increase is observed in average $<\Delta\%R_{NP}>$ for the D1-HNPs as compared to that for the HNPs without ssDNA; this large increase is attributed to both the inclusion of acrylamide-modified ssDNA into the hydrogel and its effect on the polymerization process. Specifically, the Michael addition of acrylamide to A, C,

and G nucleotides in the ssDNA assisted in the incorporation of DNA into the DNA–HNPs. However, this reaction limited the bioavailability of the ssDNA within DNA–HNPs to about 35%. Future work will focus on the further synthesis, nucleic acid/protein uptake and enzymatic activity of various ssDNA sequences, such as aptamers, in these DNA–HNPs.

3.5 Supporting Information

SYBR Green I fluorescence measurements and fluorescence loss measurements, fluorescence curve was plotted to calculate the fluorescence of the supernatant (Figure S1), statistical data for SPRI adsorption measurements, SPRI microscopy for D1c binding to D1-HNPs (Table S1) (PDF)

3.6 Acknowledgments

This work was supported by the National Science Foundation through grant CHE-1807317. DLS and nanoparticle size distribution and concentration data were acquired at the Laser Spectroscopy Facility in the Department of Chemistry at UC, Irvine. The authors would like to thank Christian Baca for his assistance in data acquisition and analysis and Dr Li Xing for her help in acquiring cryo-TEM images. Cryo-TEM work was performed at the UC Irvine Materials Research Institute (IMRI).

3.7 References

1. Zhang, Z.; Liu, J. Intracellular delivery of a molecularly imprinted peroxidase mimicking DNAzyme for selective oxidation. *Mater. Horiz.* **2018**, 5 (4), 738-744.

2. Huang, Y.; Ma, Y.; Chen, Y.; Wu, X.; Fang, L.; Zhu, Z.; Yang, C. J. Target-responsive DNAzyme cross-linked hydrogel for visual quantitative detection of lead. *Anal. Chem.* **2014,** *86* (22), 11434-11439.

3. Karimi, M.; Ghasemi, A.; Sahandi Zangabad, P.; Rahighi, R.; Moosavi Basri, S. M.; Mirshekari, H.; Amiri, M.; Shafaei Pishabad, Z.; Aslani, A.; Bozorgomid, M. *et al.* Smart micro/nanoparticles in stimulus-responsive drug/gene delivery systems. *Chem. Soc. Rev.* **2016,** *45* (5), 1457-1501.

4. Kahn, J. S.; Hu, Y.; Willner, I. Stimuli-Responsive DNA-Based Hydrogels: From Basic Principles to Applications. *Acc. Chem. Res.* **2017,** *50* (4), 680-690.

5. Peppas, N. A.; Hilt, J. Z.; Khademhosseini, A.; Langer, R. Hydrogels in Biology and Medicine: From Molecular Principles to Bionanotechnology. *Adv. Mater.* **2006,** *18* (11), 1345-1360.

6. Carvalho, W. S. P.; Wei, M.; Ikpo, N.; Gao, Y.; Serpe, M. J., Polymer-Based Technologies for Sensing Applications. *Anal. Chem.* **2018,** *90* (1), 459-479.

7. Hamidi, M.; Azadi, A.; Rafiei, P. Hydrogel nanoparticles in drug delivery. *Adv. Drug Delivery Rev.* **2008,** *60* (15), 1638-1649.

8. Vermonden, T.; Censi, R.; Hennink, W. E. Hydrogels for protein delivery. *Chem. Rev.* **2012,** *112* (5), 2853-2888.

9. Segovia, N.; Pont, M.; Oliva, N.; Ramos, V.; Borros, S.; Artzi, N. Hydrogel doped with nanoparticles for local sustained release of siRNA in breast cancer. *Adv. Healthcare Mater.* **2015,** *4* (2), 271-280.

10. Plamper, F. A.; Richtering, W. Functional Microgels and Microgel Systems. *Acc. Chem. Res.* **2017,** *50* (2), 131-140.

11. Cho, K.; Fasoli, J. B.; Yoshimatsu, K.; Shea, K. J.; Corn, R. M. Measuring Melittin Uptake into Hydrogel Nanoparticles with Near-Infrared Single Nanoparticle Surface Plasmon Resonance Microscopy. *Anal. Chem.* **2015,** *87* (9), 4973-4979.

12. O'Brien, J.; Lee, S.-H.; Gutiérrez, J. M.; Shea, K. J. Engineered nanoparticles bind elapid snake venom toxins and inhibit venom-induced dermonecrosis. *PLoS Neglected Trop. Dis.* **2018,** *12* (10), e0006736.

13. Miura, Y.; Hoshino, Y.; Seto, H. Glycopolymer Nanobiotechnology. *Chem. Rev.* **2016,** *116* (4), 1673-1692.

14. Maley, A. M.; Terada, Y.; Onogi, S.; Shea, K. J.; Miura, Y.; Corn, R. M. Measuring Protein Binding to Individual Hydrogel Nanoparticles with Single-Nanoparticle Surface Plasmon Resonance Imaging Microscopy. *J. Phys. Chem. C* **2016,** *120* (30), 16843-16849.

15. Chen, Y.; Nakamoto, K.; Niwa, O.; Corn, R. M. On-chip synthesis of RNA aptamer microarrays for multiplexed protein biosensing with SPR imaging measurements. *Langmuir* **2012,** *28* (22), 8281-8285.

16. Freeman, R.; Liu, X. Q.; Willner, I. Amplified Multiplexed Analysis of DNA by the Exonuclease III-Catalyzed Regeneration of the Target DNA in the Presence of Functionalized Semiconductor Quantum Dots. *Nano. Lett.* **2011,** *11* (10), 4456-4461.

17. Frutos, A. G.; Smith, L. M.; Corn, R. M. Enzymatic ligation reactions of DNA "words" on surfaces for DNA computing. *J. Am. Chem. Soc.* **1998,** *120* (40), 10277-10282.

18. Lilienthal, S.; Shpilt, Z.; Wang, F.; Orbach, R.; Willner, I. Programmed DNAzyme-Triggered Dissolution of DNA-Based Hydrogels: Means for Controlled Release of Biocatalysts and for the Activation of Enzyme Cascades. *ACS Appl. Mater. Interfaces* **2015,** *7* (16), 8923-8931.

19. Song, S.; Wang, L.; Li, J.; Fan, C.; Zhao, J., Aptamer-based biosensors. *TrAC, Trends Anal. Chem.* **2008,** *27* (2), 108-117.

20. Breaker, R. R.; Joyce, G. F. A DNA enzyme with Mg2+-dependent RNA phosphoesterase activity. *Chem. Biol.* **1995,** *2* (10), 655-660.

21. Moura, L. M.; Martinho, J. M. G.; Farinha, J. P. S. DNA Hybridization in Thermoresponsive Polymer Nanoparticles. *ChemPhysChem* **2010,** *11* (8), 1749-1756.

22. Fujita, M.; Hiramine, H.; Pan, P.; Hikima, T.; Maeda, M. Effects of Complementary DNA and Salt on the Thermoresponsiveness of Poly(N-isopropylacrylamide)-b-DNA. *Langmuir* **2016,** *32* (4), 1148-1154.

23. Soontornworajit, B.; Zhou, J.; Shaw, M. T.; Fan, T. H.; Wang, Y. Hydrogel functionalization with DNA aptamers for sustained PDGF-BB release. *Chem. Commun.* **2010,** *46* (11), 1857-1859.

24. Smith, M. H.; Lyon, L. A. Multifunctional nanogels for siRNA delivery. *Acc. Chem. Res.* **2012,** *45* (7), 985-993.

25. Dunn, S. S.; Tian, S.; Blake, S.; Wang, J.; Galloway, A. L.; Murphy, A.; Pohlhaus, P. D.; Rolland, J. P.; Napier, M. E.; DeSimone, J. M. Reductively responsive siRNA-conjugated hydrogel nanoparticles for gene silencing. *J. Am. Chem. Soc.* **2012,** *134* (17), 7423-7430.

26. Zeynep Atay, N.; Çalgan, D.; Özakat, E.; Varnali, T. Acrylamide and glycidamide adducts of Guanine. *J. Mol. Struct.: THEOCHEM* **2005,** *728* (1), 249-251.

27. Besaratinia, A.; Pfeifer, G. P. DNA adduction and mutagenic properties of acrylamide. *Mutat. Res., Genet. Toxicol. Environ. Mutagen.* **2005,** *580* (1), 31-40.

28. Watzek, N.; Böhm, N.; Feld, J.; Scherbl, D.; Berger, F.; Merz, K. H.; Lampen, A.; Reemtsma, T.; Tannenbaum, S. R.; Skipper, P. L.; Baum, M.; Richling, E.; Eisenbrand, G. N7-Glycidamide-Guanine DNA Adduct Formation by Orally Ingested Acrylamide in Rats: A dose–

response Study Encompassing Human Diet-Related Exposure Levels. *Chem. Res. Toxicol.* **2012,** *25* (2), 381-390.

29. Huang, S.; Lu, S.; Huang, C.; Sheng, J.; Zhang, L.; Su, W.; Xiao, Q., An electrochemical biosensor based on single-stranded DNA modified gold electrode for acrylamide determination. *Sens. Actuators, B* **2016,** *224* (C), 22-30.

30. Freeman, R.; Han, M.; Álvarez, Z.; Lewis, J. A.; Wester, J. R.; Stephanopoulos, N.; McClendon, M. T.; Lynsky, C.; Godbe, J. M.; Sangji, H. *et al.* Reversible self-assembly of superstructured networks. *Science* **2018,** *362* (6416), 808-813.

31. Halpern, A. R.; Wood, J. B.; Wang, Y.; Corn, R. M. Single-nanoparticle near-infrared surface plasmon resonance microscopy for real-time measurements of DNA hybridization adsorption. *ACS Nano* **2014,** *8* (1), 1022-1030.

32. Maley, A. M.; Lu, G. J.; Shapiro, M. G.; Corn, R. M. Characterizing Single Polymeric and Protein Nanoparticles with Surface Plasmon Resonance Imaging Measurements. *ACS Nano* **2017,** *11* (7), 7447-7456.

33. Zybin, A.; Kuritsyn, Y. A.; Gurevich, E. L.; Temchura, V. V.; Uberla, K.; Niemax, K. Real-time Detection of Single Immobilized Nanoparticles by Surface Plasmon Resonance Imaging. *Plasmonics* **2010,** *5* (1), 31-35.

34. Wang, W.; Tao, N. Detection, counting, and imaging of single nanoparticles. *Anal. Chem.* **2014,** *86* (1), 2-14.

35. Yu, H.; Shan, X.; Wang, S.; Tao, N. Achieving High Spatial Resolution Surface Plasmon Resonance Microscopy with Image Reconstruction. *Anal. Chem.* **2017,** *89* (5), 2704-2707.

36. Solomon, J. J.; Fedyk, J.; Mukai, F.; Segal, A. Direct Alkylation of 2′-Deoxynucleosides and DNA following *in Vitro* Reaction with Acrylamide. *Cancer Res.* **1985,** *45*, 3465-3470.

37. Gruber, A. R.; Lorenz, R.; Bernhart, S. H.; Neuböck, R.; Hofacker, I. L. The Vienna RNA websuite. *Nucleic Acids Res.* **2008,** *36* (Web Server issue), W70-W74.

Chapter 4

Fabrication and Characterization of Bioactive Nanocomposite Hydrogel Nanoparticles.

4.1 Introduction

Hydrogel nanoparticles have been incorporated in a variety of scientific endeavors, ranging from capture and detection through molecular recognition,[1-4] to the formation of composite materials with other inorganic components to act as sensors.[5-9] Additionally, hydrogel nanoparticles can be tuned to uptake and release cargo unique to a particular monomer incorporation.[10-13] For example, the Willner group has performed research in using DNAzymes as release mechanisms within their hydrogel nano- and micro-scale structures.[2, 14] Separately, HNPs have made use of numerous inorganic nanoparticles to aid in the opening or closing of the polymer pores,[15] drug delivery,[16-17] and to provide advanced signal enhancement, thereby lowering the levels of detection in a system.[18-20]

Showing a plethora of possibilities, hydrogel-based assemblies have explored additional functionality through the use of DNA incorporation. DNA-based hydrogels have been shown to uptake and deliver RNA,[21] use DNA to expand upon HNP cargo-loading capabilities,[22] and generally be bioavailable targets.[23] In particular, the previous chapter sought to more fully explore the integration of DNA into HNP systems and demonstrated bioactive DNA that had been integrated into the polymer backbone.[24] DNA integration was predominately achieved through the polymerization of the acrylic phosphoramidite group on the 5' end of the DNA, but also through Michael addition reactions between the acrylic monomers and the bases guanine, cytosine, and adenine.[25-27]

In this chapter, the synthesis, characterization, and application of ferrite magnetic nanoparticles encapsulated within HNPs were examined, both with and without DNA incorporation. The ferrite-encapsulated HNPs were shown to have a degree of magnetic properties, resulting in magnetic nanocomposites.[28] Their potential as a purification method via

particle aggregation induced by an external magnetic field is explored through the analysis of surface plasmon resonance imaging (SPRI) measurements.[3, 29] This chapter aims to both examine the versatility of these systems and demonstrate that these structures retain their bioactivity even in the presence of the magnetic structures. In exploring the potential of bioactive nanocomposite particles, our hope is to analyze alternative solution isolation and separation purification methods that are gentler than methods that rely on centrifugal force.[30-31]

4.2 Methods and Materials

4.2.1 Ferrite Nanoparticles.

Ferrite nanoparticles were synthesized and characterized as outlined in a separate manuscript in process. A ligand exchange modified from Zhang was then performed to yield polyacrylic acid coated nanoparticles.[32] A final solution of these polyacrylic acid-coated ferrite nanoparticles was used as is for HNP incorporation for the remainder of the chapter.

4.2.2 Hydrogel Nanoparticle Materials.

N-isopropylacrylamide (NIPAm), acrylic acid (AAc), sodium dodecyl sulfate (SDS), and ammonium persulfate (APS) were obtained from Sigma-Aldrich, Inc. (St. Louis, MO). N,N-methylenebis(acrylamide) (BIS) was obtained from Fluka (St. Louis, MO). N-tert-butylacrylamide (TBAm) was obtained from Acros Organics (Geel, Belgium). All DNA were purchased from Integrated DNA Technologies (Coralville, IA). NIPAm was recrystallized from hexane before use. All other chemicals were used as received.

4.2.3 Hydrogel Nanoparticle Synthesis.

HNP synthesis was adapted from the procedure detailed in Matthews.[24] The monomers NIPAm (53 mol %), TBAm (38 mol %), AAc (5 mol %), and BIS (2 mol %) were dissolved in 1.7 mL of nanopure water in a round-bottom flask for a total monomer concentration of 21 mM.

TBAm was dissolved in 50 μL of ethanol before addition to the monomer solution. The surfactant SDS (0.25 mg) was also added to the monomer solution to control nanoparticle size. Nitrogen gas was bubbled through the solution for 30 minutes. Following the addition of a 100 μL aqueous solution containing 1 mg of APS, the polymerization reaction was carried out for 3 hours in an oil bath preset to 60 °C. For ferrite-encapsulation HNP synthesis, 100 μL of the diluted ferrite solution was added to the aqueous solution after thirty minutes of reaction time. From there, the reaction was permitted to continue for an additional 2.5 hours under nitrogen atmosphere. When forming ferrite-encapsulated DNA-HNPs, 100 μL of dilute ferrite solution was added approximately 20 minutes after the start of the reaction, followed by the addition of 1.3 μmol (1 mM aqueous solution) of DNA to the reaction flask via syringe 40 minutes after the start of the reaction synthesis. The polymerization reaction was left to be completed for an additional 2.5 hours under nitrogen atmosphere.

All of the resulting solutions were independently purified by dialysis using a 12-14 kDa molecular weight cut off dialysis membrane against an excess amount of nanopure water (changed three times a day) for three days. Hydrogel nanoparticle size distribution and concentration were measured in aqueous solutions at 25 °C on a NanoSight NS300 Nanoparticle Tracking and Analysis microscopy system (Malvern Panalytical). Cryo-EM images were obtained using 3μL of sample solution applied on a glow-discharged Quantifoil grid (Quantifoild, R2/2) and then loaded on Leica EMGP plunger (Leica Biosystem). The grid was quickly plunged into liquid propane after blotting away the excess liquid and the hydrogel particles were then embedded in a thin layer of vitrified ice on the grid. The cryo-grid was then transferred into a JEM-2100F electron microscope using a Gatan cryo-transfer holder (Gatan, Inc). The electron microscope was operated at 200KV with a field emission gun and specimen

was examined under minimum dose system. The images were recorded on a OneView camera (Gatan, Inc.) at 40,000X magnification, corresponding to 0.28nm per pixel at specimen space.

4.2.4 Substrate Preparation.

The Au substrates were coated by thermal vapor deposition of a 1 nm Cr adhesion layer and 45 nm Au onto borosilicate No. 1.5 coverslips (Fisherbrand, Pittsburgh, PA). For ferrite-encapsulated HNP measurements, the Au surface was immobilized with 11-mercaptoundecylamine (MUAM, Dojindo, Japan) by immersing the Au substrate into a 1 mM MUAM/EtOH solution. Unmodified HNPs and DNA-HNPs used a 1 mM 1-undecanethiol (C11) ethanol solution. All Au surface was separated using adhesive silicon isolation wells (Electron Microscopy Sciences, Hatfield, PA).

4.2.5 SPRI Microscopy Measurements.

The SPRI microscope setup follows a previous publication where the single-nanoparticle microscope was built into the frame of an IX51 inverted microscope (Olympus, Tokyo, Japan).[33] A 1 mW, 814 nm diode laser (Melles Griot, Carlsbad, CA) was expanded and collimated using a spatial filter (Newport Corp., Newport Beach, CA). The beam was polarized and focused with a lens (f = 200 mm) and then directed onto the back focal plane of a 100× 1.49 high numerical aperture objective (Olympus). The beam was directed upward near the edge of the objective by a gold-coated knife-edge mirror (Thorlabs, Newton, NJ). The reflected image was passed out the other side of the objective and acquired by an Andor Neo sCMOS camera (South Windsor, CT). Each three-second reflectivity image was acquired by accumulating 30 11-bit, 0.1 s exposures.

4.3 Results and Discussion

4.3.1 Characterization of Ferrite Nanoparticles

For the purposes of this project, ferrite nanoparticles were solely characterized by TEM. STEM HAADF images were acquired to characterize their individual size and shape distributions. As shown in Figure 4.1, the ferrite nanoparticles before ligand exchange show uniformity in their size and shape, here estimated to average 40 nm by image analysis. Further focusing on an individual nanoparticle, the crystalline structure can be readily seen, confirming that they are single crystals in nature.

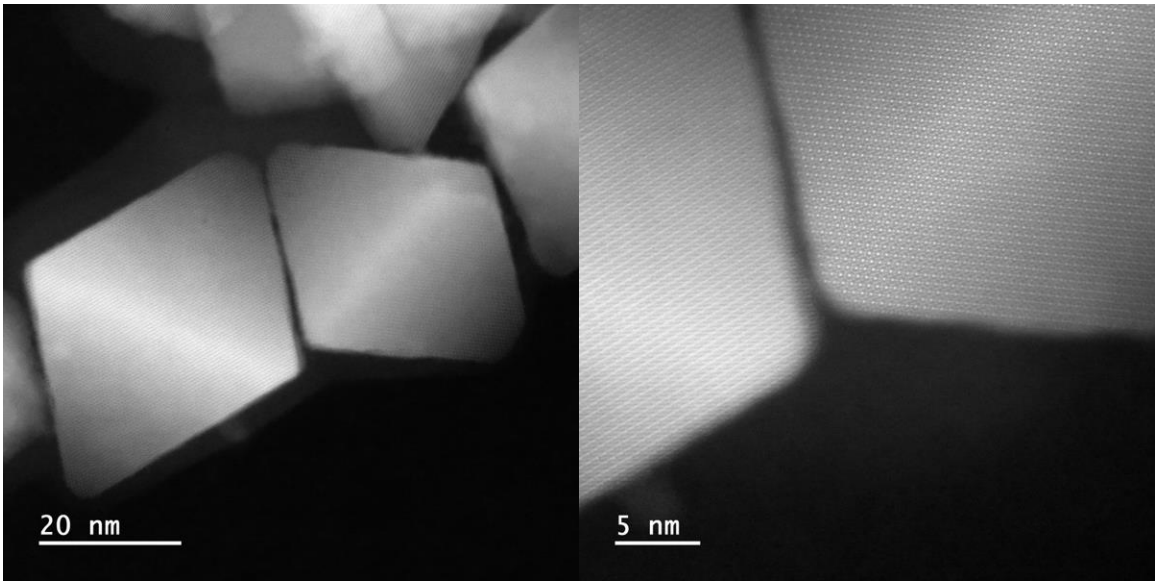

Figure 4.1: Grand Arm TEM of a) individual ferrite nanoparticles and b) a zoomed in image displaying the crystalline structure.

In order to make the ferrite nanoparticles soluble in water, thus encouraging encapsulation by the hydrogel nanoparticles, a ligand-exchange was performed. Rather than maintaining rigid corners, Figure 4.2 shows a rounding of the nanoparticles post-exchange, indicating the possible presence of a thin-layer polyacrylic acid coating.

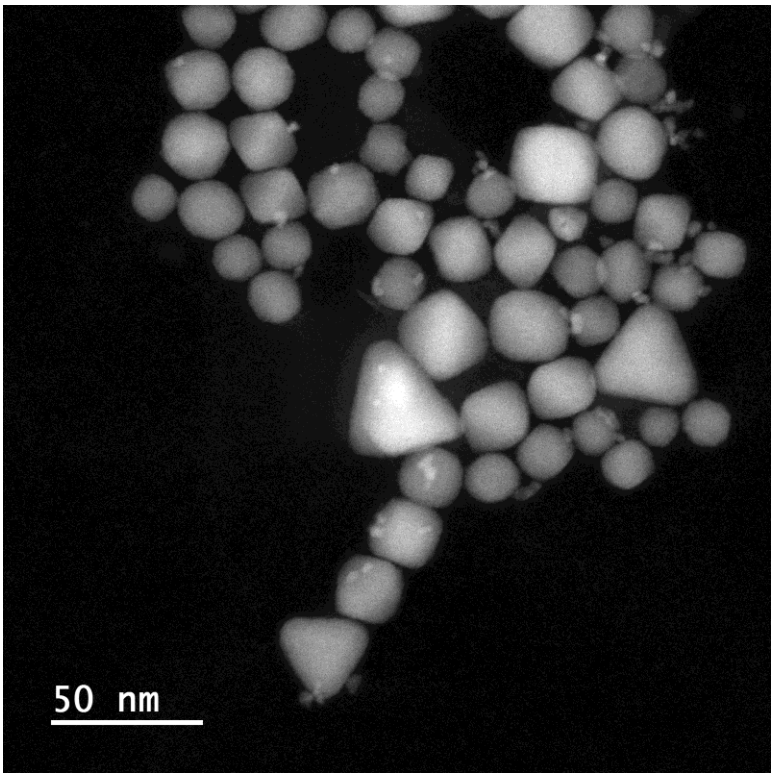

Figure 4.2: TEM image of polyacrylic acid-coated ferrite nanoparticles.

4.3.2 Ferrite-encapsulated HNPs synthesis and characterization

Four separate batches of HNPs solutions were prepared: unmodified HNPs, HNPs that contain a polymerized DNA sequence, HNPs that have ferrite encapsulated, and ferrite-encapsulated HNPs that have DNA polymerized into its backbone structure. The selected DNA sequence used is a modified 30mer sequence from Lilienthal, et. al.,[2] and has been used in our previous DNA-HNP paper.[24]

The primary method of characterization for the collection of HNPs and its derivatives was near-infrared single-nanoparticle SPRI microscopy. Similar to data observed when characterizing a variety of particle types (gas vesicles, polymeric nanostructures, and metal nanoparticles),[34] point diffractions are created due to the *in-situ* adsorption of HNPs to a hydrophobic gold surface. Upon exposure to the target solution, SPRI reflectivity images are obtained every 3 s over a 10 min collection interval. The images are sequentially subtracted,

forming a set of 200 SPRI differential reflectivity (Δ%R) images.

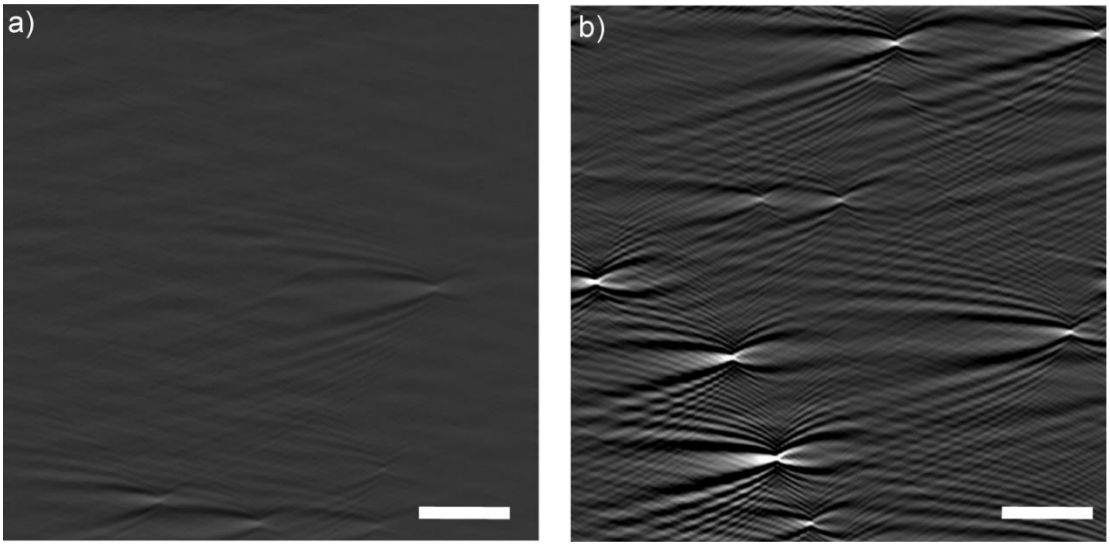

Figure 4.3: Example of SPRI differential reflectivity images of a) HNPs and b) ferrite-encapsulated HNPs, irreversibly adsorbing to gold thin-film surfaces. The scale bar for both images is 10 μm.

Two such examples of these differential reflectivity images are shown in Figure 4.4. Two sets of chemically modified gold thin-films were used dependent on the type of HNPs analyzed. For ferrite-encapsulated HNPs, a MUAM surface was used, whereas the other types of HNPs examined in this chapter all used a C11 modified surface. The intensity of each binding event is dictated by the interaction of the nanoparticle refractive index and the traveling SPPs, of which the shape and intensity of these patterns have been elaborated upon previously. Here, the discrepancy between signal intensity shown between the unmodified HNPs of Figure 4.4a and that of ferrite-encapsulated HNPs in Figure 4.4b can be attributed to the presence of ferrite.

Table 4.1. Hydrodynamic Size Measurements from DLS for Hydrogel Nanoparticles and Statistics from Single-Nanoparticle SPRI measurements

nanoparticle	diameter (nm)	$\langle \Delta\%R_{NP} \rangle$	standard deviation (s)	95% CI	# of NPs
HNPs	196 ± 1	0.48	0.18	0.02	402
DNA- HNPs	202 ± 2	2.38	1.17	0.11	424
Ferrite-HNPs	208 ± 1	6.1	2.2	0.21	438
Ferrite DNA-HNPs	193 ± 1	3.6	1.5	0.14	422
Ferrite DNA-HNPs + 10 nM cDNA	-	2.9	1.3	0.14	375

Figure 4.5 plots the $\Delta\%R_{NP}$ values obtained from the two different types of HNPs compositions. Figure 4.5a shows the real-time binding events for each HNP irreversibly adsorbing to the surface and the resulting $\Delta\%R_{NP}$ signal for HNPs and ferrite-encapsulated HNPs, both as a function of time. Figure 4.5b is the total frequency distribution for each case. Overall, the unmodified HNPs demonstrated a comparable $\Delta\%R_{NP}$ to our previously published results, yielding a $\langle \Delta\%R_{NP} \rangle$ average value of 0.48 ± 0.02%. In contrast, with the addition of only ferrite to the synthesis, a drastic $\langle \Delta\%R_{NP} \rangle$ shift occurred, yielding a value of 6.1 ± 0.21%. In both instances, the average hydrodynamic diameter is roughly the same, 196 ± 1 nm and 208 ± 1 nm, respectfully. As a result, we attribute the increase in signal as a whole to the presence of ferrite nanoparticles clustered within the HNPs. Additionally, these ferrite nanoparticles cannot be detected individually on the microscope. It is only when confined within the HNPs that this signal change arises.

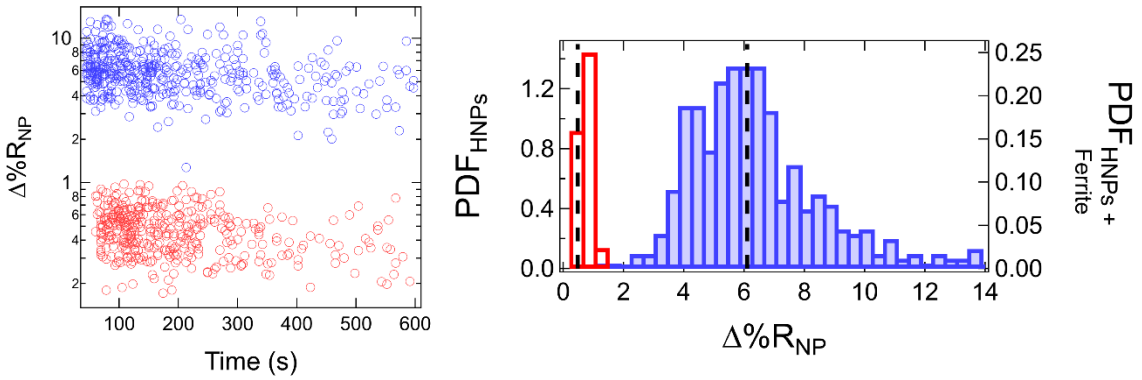

Figure 4.4: a) Time dependent distribution of Δ%R values of HNPs (red) and ferrite-encapsulated HNPs (blue) over time, measured each in separate experiments. Each circle represents a single irreversible binding event of an HNP to the chemically modified surface. b) Δ%R frequency distributions of HNPs (red) and ferrite-encapsulated HNPs (blue). The averages for each distribution are denoted by the black dotted line, and are 0.48 ± 0.02 and 6.1 ± 0.21 %, respectively.

The average Δ%R values of the two types of HNPs were also corroborated by using Cryo-EM images. Summarized in Figure 4.6, the images show individual particles, and not aggregates, of both a) hydrogel nanoparticles and b) ferrite-HNPs. The ferrite-HNP particles were initially concentrated using an external magnet to isolate them before taking an aliquot to image later. The preparation technique parallels the single-nanoparticle SPRI preparation, leading us to believe that the cryo-EM images accurately correspond to the <Δ%R> values obtained. The image also reveals a variation in the number of encapsulated ferrite nanoparticles, explaining the wider Δ%R distribution in comparison to unmodified HNPs. Thus, the large change in the average Δ%R values can be attributed to the clustering of the ferrite within the HNPs.

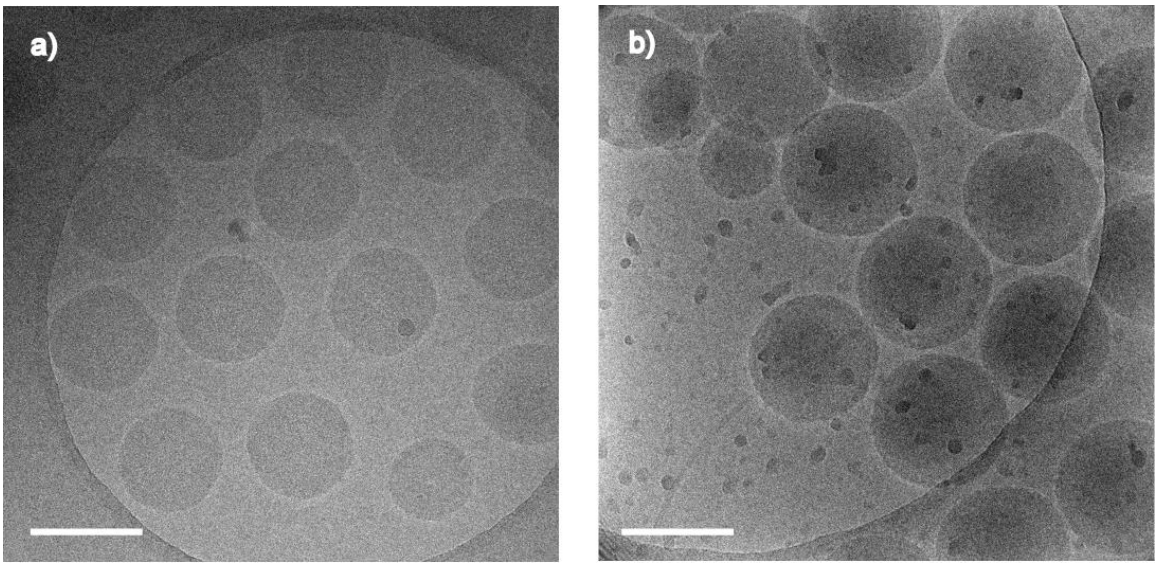

Figure 4.5: Cryo-EM image of vitrified a) hydrogel nanoparticles and b) ferrite-encapsulated HNPs. The scale bar is 200 nm.

3.3.4 DNA incorporation when forming composite nanoparticles

Figure 4.6 plots the $\Delta\%R_{NP}$ values of DNA-HNPs ferrite against a) ferrite-encapsulated HNPs and b) DNA-HNPs, with the averages for each distribution denoted by the black dotted lines. Rather than observing an even greater increase in the $<\Delta\%R_{NP}>$ for ferrite-encapsulated DNA-HNPs, the opposite occurred: the average value of the ferrite-encapsulated DNA-HNPs, when compared to ferrite HNPs, dropped from 6.1 ± 0.21% to 3.6 ± 0.14%. Additionally, the distribution of values more greatly mirrors that of the DNA-HNPs distribution.

This large signal decrease suggests numerous effects occurring simultaneously within the HNPs. First, the ferrite nanoparticles themselves are not covalently fixed within the polymer matrix. Rather, these nanoparticles are thought to be held in place by the electrostatic interaction between the polyacrylic acid coating and the charged acrylic acid monomer, as well as orienting the ferrite within the matrix such that unfavorable interactions between polar and nonpolar species are minimized. When incorporating DNA into the backbone of the polymer in the presence of ferrite, however, it is likely the ferrite nanoparticles are partially being ejected in

favor of the DNA. This is most likely due to both the covalent attachment of the DNA to the polymer backbone due to its phosphoramidite functional group, as well as Michael addition which has been shown to assist in the incorporation of DNA into the polymer. Additionally, same charge repulsion effects between the polyacrylic acid ferrite and the now polymerized DNA could also play a role in the decreased amount of ferrite nanoparticles present within the HNPs, translating directly to a drop in average signal. It should be noted some ferrite is still present, as the average signal for ferrite-encapsulated DNA-HNPs is still more than a full percent higher than the DNA-HNPs with the identical sequence. Therefore, the number of ejected ferrite-nanoparticles is most likely dependent on the type of DNA sequence used, due to the additional effects of Michael addition effectiveness based on base pairs, as well as the overall length, effecting the influence of same charge repulsion occurring.

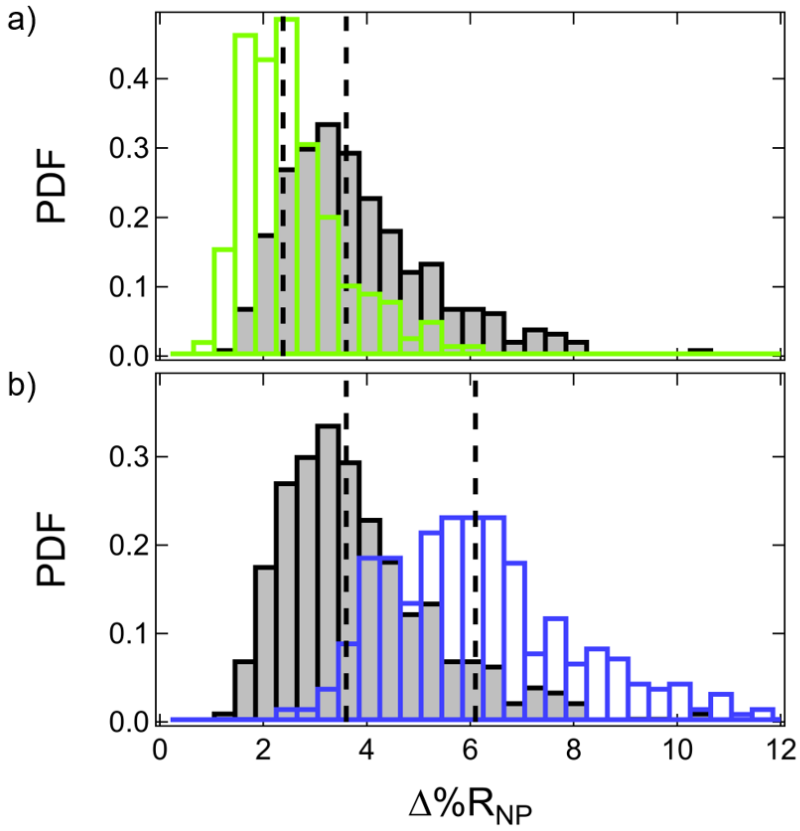

Figure 4.6: Single-nanoparticle SPRI distribution frequencies comparing ferrite-encapsulated DNA-HNPs (black) to a) DNA-HNPs (green) and b) ferrite-HNPs (blue). The dotted black lines within each distribution marks the averages of each type of HNP.

Similar effects were observed with the addition of complementary DNA to the system. Figure 4.7 plots the addition of 10 nM cDNA to ferrite-encapsulated DNA-HNPs against a) unhybridized ferrite-encapsulated DNA-HNPs and b) ferrite HNPs. Again, there is a further decrease in the average $<\Delta\%R_{NP}>$, dropping down to now 2.9 ± 0.14%. This further emphasizes the ejection of ferrite nanoparticles from the HNPs in place of cDNA, most likely due to the combination of charge repulsions and physical presence. However, this does indicate that the nanocomposite HNPs can still be readily bioactive between a probe molecule and its specific target. When control experiments were performed with non-complementary DNA again at 10 nM, the resulting signal for the ferrite-encapsulated DNA-HNPs remained relatively unchanged.

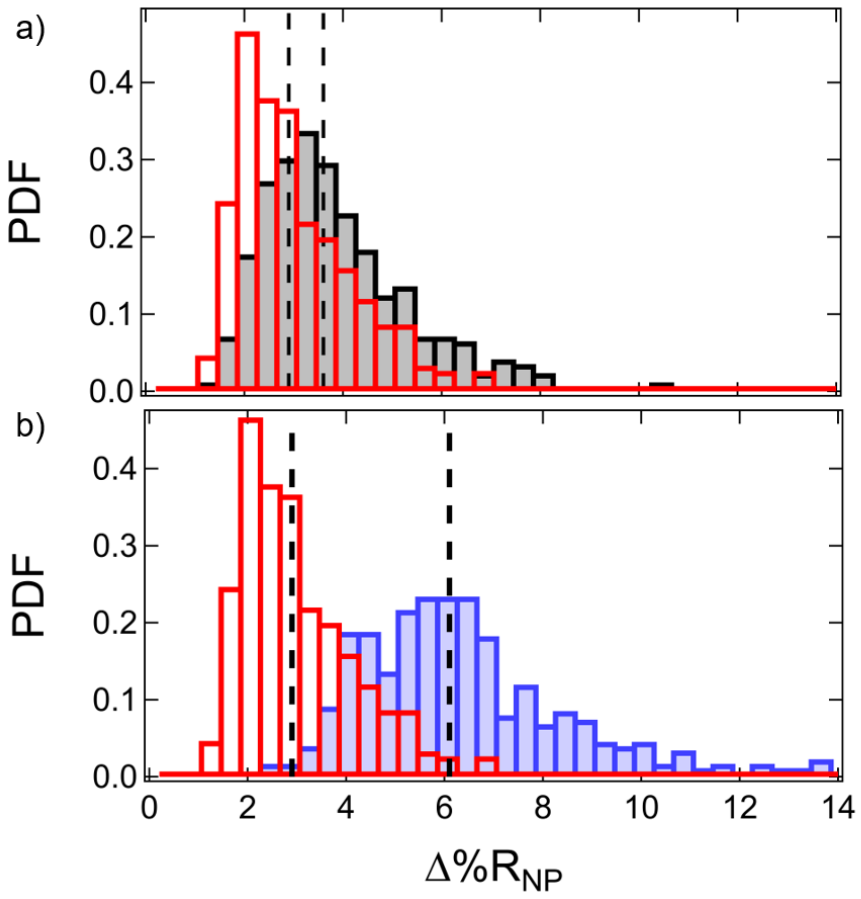

Figure 4.7: Comparison of single-nanoparticle SPRI frequency distributions. Ferrite-encapsulated DNA-HNPs after the addition of 10 nM cDNA (red) were plotted against a) ferrite-encapsulated DNA-HNPs (black) and b) ferrite-encapsulated HNPs (blue). The averages of each distribution for both sets of data are denoted by the dotted black line.

4.4 Conclusion

In this chapter, both ferrite-encapsulated HNPs and DNA-HNPs were synthesized. Cryo-EM and SPRI frequency distributions show successful incorporation, and displacement by the inclusion of DNA into the polymer matrix. In the future, increasing the retention and stability of the ferrite in the presence of DNA will be explored by examining ferrite incorporate relative to DNA sequence length and composition. Altering the polymer coating of the ferrites a net positive charged surface will also be explored to elucidate particle retention via charge attraction.

Lastly, we will examine other potential composite nanoparticle formations as a means of cargo loading and de-loading. For example, the use of gold nanoparticles to induce phase transitions for the HNPs when exposed to a laser source.

4.5 Acknowledgments

This work was supported by the National Science Foundation through grant CHE-1807317. DLS and nanoparticle size distribution and concentration data were acquired at the Laser Spectroscopy Facility in the Department of Chemistry at UC, Irvine. Cryo-TEM work was performed at the UC Irvine Materials Research Institute (IMRI).

4.6 References

1. Dave, N.; Chan, M. Y.; Huang, P. J.; Smith, B. D.; Liu, J., Regenerable DNA-functionalized hydrogels for ultrasensitive, instrument-free mercury(II) detection and removal in water. J. Am. Chem. Soc. 2010, 132 (36), 12668-12673.

2. Lilienthal, S.; Shpilt, Z.; Wang, F.; Orbach, R.; Willner, I., Programmed DNAzyme-Triggered Dissolution of DNA-Based Hydrogels: Means for Controlled Release of Biocatalysts and for the Activation of Enzyme Cascades. ACS Appl. Mater. Interfaces. 2015, 7 (16), 8923-8931.

3. Maley, A. M.; Terada, Y.; Onogi, S.; Shea, K. J.; Miura, Y.; Corn, R. M., Measuring Protein Binding to Individual Hydrogel Nanoparticles with Single-Nanoparticle Surface Plasmon Resonance Imaging Microscopy. J. Phys. Chem. C. 2016, 120 (30), 16843-16849.

4. Plamper, F. A.; Richtering, W., Functional Microgels and Microgel Systems. Acc. Chem. Res. 2017, 50 (2), 131-140.

5. Baeissa, A.; Dave, N.; Smith, B. D.; Liu, J., DNA-functionalized monolithic hydrogels and gold nanoparticles for colorimetric DNA detection. ACS Appl. Mater. Interfaces. 2010, 2 (12), 3594-3600.

6. Kahn, J. S.; Hu, Y.; Willner, I., Stimuli-Responsive DNA-Based Hydrogels: From Basic Principles to Applications. Acc. Chem. Res. 2017, 50 (4), 680-690.

7. Lopez, A.; Liu, J., Self-Assembly of Nucleobase, Nucleoside and Nucleotide Coordination Polymers: From Synthesis to Applications. ChemNanoMat 2017, 3 (10), 670-684.

8. Zhang, Q.; Serpe, M. J.; Mugo, S. M., Stimuli Responsive Polymer-Based 3D Optical Crystals for Sensing. Polymers 2017, 9 (11), 436.

9. Li, W.; Hu, L.; Zhu, J.; Li, D.; Luan, Y.; Xu, W.; Serpe, M. J., Comparison of the Responsivity of Solution-Suspended and Surface-Bound Poly(N-isopropylacrylamide)-Based Microgels for Sensing Applications. ACS Appl. Mater. Interfaces 2017, 9 (31), 26539-26548.

10. Moura, L. M.; Martinho, J. M. G.; Farinha, J. P. S., DNA Hybridization in Thermoresponsive Polymer Nanoparticles. ChemPhysChem 2010, 11 (8), 1749-1756.

11. Wang, D.; Hu, Y.; Liu, P.; Luo, D., Bioresponsive DNA Hydrogels: Beyond the Conventional Stimuli Responsiveness. Acc. Chem. Res. 2017, 50 (4), 733-739.

12. Zhang, Z.; Liu, B.; Liu, J., Molecular Imprinting for Substrate Selectivity and Enhanced Activity of Enzyme Mimics. Small 2017, 13 (7), 1602730.

13. Carvalho, W. S. P.; Wei, M.; Ikpo, N.; Gao, Y.; Serpe, M. J., Polymer-Based Technologies for Sensing Applications. Anal. Chem. 2018, 90 (1), 459-479.

14. Guo, W.; Lu, C. H.; Qi, X. J.; Orbach, R.; Fadeev, M.; Yang, H. H.; Willner, I., Switchable bifunctional stimuli-triggered poly-N-isopropylacrylamide/DNA hydrogels. Angew. Chem. Int. Ed. Engl. 2014, 53 (38), 10134-10138.

15. Peppas, N. A.; Hilt, J. Z.; Khademhosseini, A.; Langer, R., Hydrogels in Biology and Medicine: From Molecular Principles to Bionanotechnology. Adv. Mater. 2006, 18 (11), 1345-1360.

16. Soontornworajit, B.; Zhou, J.; Shaw, M. T.; Fan, T. H.; Wang, Y., Hydrogel functionalization with DNA aptamers for sustained PDGF-BB release. Chem. Commun. (Camb) 2010, 46 (11), 1857-9.

17. Smits, F. C.; Buddingh, B. C.; van Eldijk, M. B.; van Hest, J. C., Elastin-like polypeptide based nanoparticles: design rationale toward nanomedicine. Macromol. Biosci. 2015, 15 (1), 36-51.

18. Contreras-Cáceres, R.; Sánchez-Iglesias, A.; Karg, M.; Pastoriza-Santos, I.; Pérez-Juste, J.; Pacifico, J.; Hellweg, T.; Fernández-Barbero, A.; Liz-Marzán, L. M., Encapsulation and Growth of Gold Nanoparticles in Thermoresponsive Microgels. Adv. Mater. 2008, 20 (9), 1666-1670.

19. Morones, J. R.; Frey, W., Room temperature synthesis of an optically and thermally responsive hybrid PNIPAM–gold nanoparticle. J. Nanoparticle Res. 2009, 12 (4), 1401-1414.

20. Kim, J. H.; Boote, B. W.; Pham, J. A.; Hu, J.; Byun, H., Thermally tunable catalytic and optical properties of gold-hydrogel nanocomposites. Nanotechnology 2012, 23 (27), 275606.

21. Song, J.; Lee, M.; Kim, T.; Na, J.; Jung, Y.; Jung, G. Y.; Kim, S.; Park, N., A RNA producing DNA hydrogel as a platform for a high performance RNA interference system. Nature Communications 2018, 9 (1), 4331.

22. Fujita, M.; Hiramine, H.; Pan, P.; Hikima, T.; Maeda, M., Effects of Complementary DNA and Salt on the Thermoresponsiveness of Poly(N-isopropylacrylamide)-b-DNA. Langmuir 2016, 32 (4), 1148-1154.

23. Maeda, M., Sequence-Specific Aggregation Behavior of DNA-Carrying Colloidal Nanoparticles Prepared from Poly(N-isopropylacrylamide)-graft-Oligodeoxyribonucleotide. Polym. J. 2006, 38 (11), 1099-1104.

24. Matthews, B. M.; Maley, A. M.; Kartub, K. M.; Corn, R. M., Characterizing the Incorporation of DNA into Single NIPAm Hydrogel Nanoparticles with Surface Plasmon Resonance Imaging Measurements. J. Phys. Chem. C. 2019, 123 (10), 6090-6096.

25. Zeynep Atay, N.; Çalgan, D.; Özakat, E.; Varnali, T., Acrylamide and glycidamide adducts of Guanine. Journal of Molecular Structure: THEOCHEM 2005, 728 (1), 249-251.

26. Besaratinia, A.; Pfeifer, G. P., DNA adduction and mutagenic properties of acrylamide. Mutat. Res., Genet. Toxicol. Environ. Mutagen. 2005, 580 (1), 31-40.

27. Solomon, J. J.; Fedyk, J.; Mukai, F.; Segal, A., Direct Alkylation of 2′-Deoxynucleosides and DNA following in Vitro Reaction with Acrylamide. Cancer Res. 1985, 45, 3465-3470.

28. Szyndler, M. W.; Corn, R. M., Self-Assembly of Flux-Closure Polygons from Magnetite Nanocubes. J. Phys. Chem. Lett. 2012, 3 (17), 2320-2325.

29. Cho, K.; Fasoli, J. B.; Yoshimatsu, K.; Shea, K. J.; Corn, R. M., Measuring Melittin Uptake into Hydrogel Nanoparticles with Near-Infrared Single Nanoparticle Surface Plasmon Resonance Microscopy. Anal. Chem. 2015, 87 (9), 4973-4979.

30. Wang, Y.; Dostalek, J.; Knoll, W., Magnetic Nanoparticle-Enhanced Biosensor Based on Grating-Coupled Surface Plasmon Resonance. Anal. Chem. 2011, 83 (16), 6202-6207.

31. Wang, J.; Munir, A.; Zhu, Z.; Zhou, H. S., Magnetic Nanoparticle Enhanced Surface Plasmon Resonance Sensing and Its Application for the Ultrasensitive Detection of Magnetic Nanoparticle-Enriched Small Molecules. Anal. Chem. 2010, 82 (16), 6782-6789.

32. Zhang, T.; Ge, J.; Hu, Y.; Yin, Y., A General Approach for Transferring Hydrophobic Nanocrystals into Water. Nano. Lett. 2007, 7 (10), 3203-3207.

33. Halpern, A. R.; Wood, J. B.; Wang, Y.; Corn, R. M., Single-nanoparticle near-infrared surface plasmon resonance microscopy for real-time measurements of DNA hybridization adsorption. ACS Nano 2014, 8 (1), 1022-30.

34. Maley, A. M.; Lu, G. J.; Shapiro, M. G.; Corn, R. M., Characterizing Single Polymeric and Protein Nanoparticles with Surface Plasmon Resonance Imaging Measurements. ACS Nano 2017, 11 (7), 7447-7456.

Appendix A

Supporting Information for Chapter 3: Characterizing the Incorporation of DNA into Single NIPAm Hydrogel Nanoparticles with Surface Plasmon Resonance Imaging Measurements

A.1 Fluorescence Loss Measurements

Fluorescence spectra were obtained using a JASCO FP-6300 Spectrofluorometer (JASCO Analytical Instruments, Easton, MD). For SYBR Green staining experiments, parallel solutions of a 1 to 10 dilution of D1-HNPs were mixed with either 10 nM D1c or D1nc, and permitted to sit for 30 minutes. Following, SYBR Green was added to a final concentration of 0.003x and allowed to sit for an additional 30 minutes. To remove excess unbound ssDNA or SYBR Green, Amicon Ultra – 0.5 mL Centrifugal Filter Devices 50k NMWL (MilliporeSigma, Burlington, MA) were used. Filters were pre-rinsed with buffer and centrifuged at 14,000 × g for 15 minutes. 200 μL of D1-HNP mixtures were then added to the filters and centrifuged three times at 14,000 × g for 15 minutes. Each wash cycle was resuspended to 200 μL total volume, and D1-HNPs were recovered from the filters by spinning at 1,000 × g for 2 minutes after the final wash. The collected mixture was brought to a total volume of 200 μL, and fluorescence measured. For fluorescence loss measurements, a standard curve was made using D1c fluorescently labeled DNA (D1c*) from 0 to 10 nM. Then, three 10 nM D1c*, 1 to 10 dilution of D1-HNPs mixtures were prepared and brought to a final volume of 1 mL. After half an hour, the mixtures were spun at 14,000 rpm for 15 minutes to create a HNP pellet at the bottom of the vial. The supernatant was removed and measured.

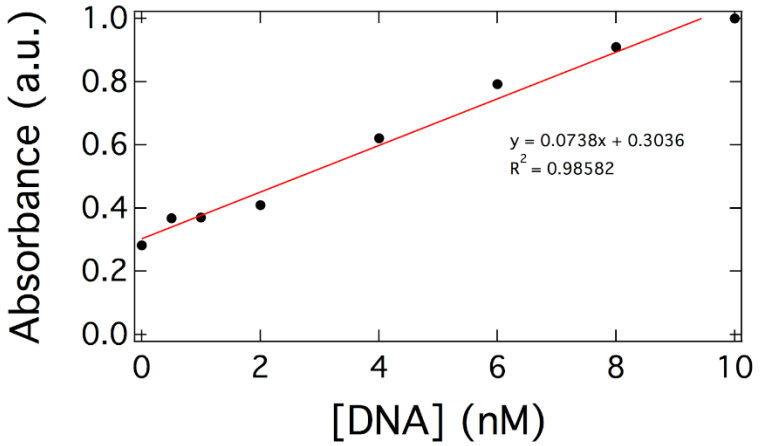

Figure A.1. A fluorescence curve was plotted to calculate the fluorescence of the supernatant. Approximately 35% of fluorescently labeled DNA was hybridized into D1-HNP, equal to 3.47 nM of accessible ssDNA within the HNP.

A.2 Statistical Analysis of SPRI Microscopy of Complementary DNA Hybridization

Table A.1. SPRI Microscopy for D1c binding to D1-HNPs.

D1c concentration (nM)	**$<\Delta\%R_{NP}>$**	**standard deviation (s)**	**95% CI**	**# of NPs**
0.1	5.60	1.84	0.22	276
1	5.94	2.20	0.26	282
3	6.75	2.60	0.30	414
5	7.02	3.11	0.35	304
10	6.98	2.40	0.27	307
100	7.11	2.20	0.25	314

A.3 DNA Incorporation into NIPAm Hydrogel Nanoparticles via Direct Michael Addition

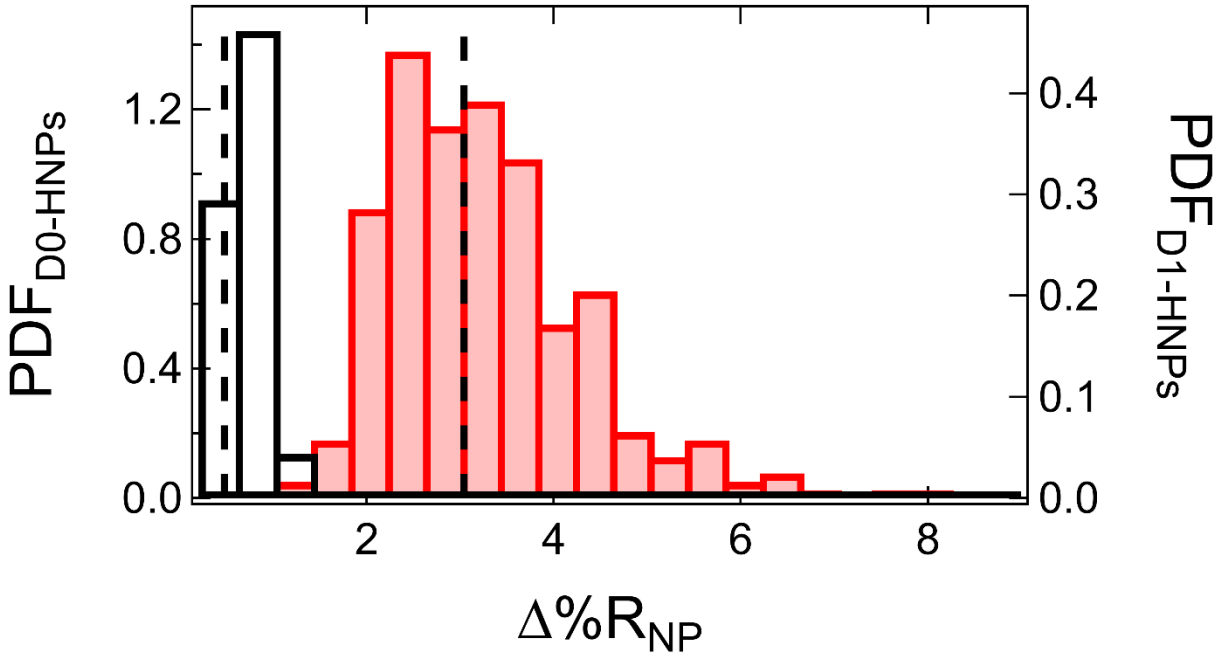

Figure A.2 Δ%R frequency distribution histogram obtained from the SPRI adsorption measurements of HNPs (black) and DNA-HNPs formed via Michael addition (red). The averages are 0.51 ± 0.02 and 3.0 ± 0.12%, respectively.

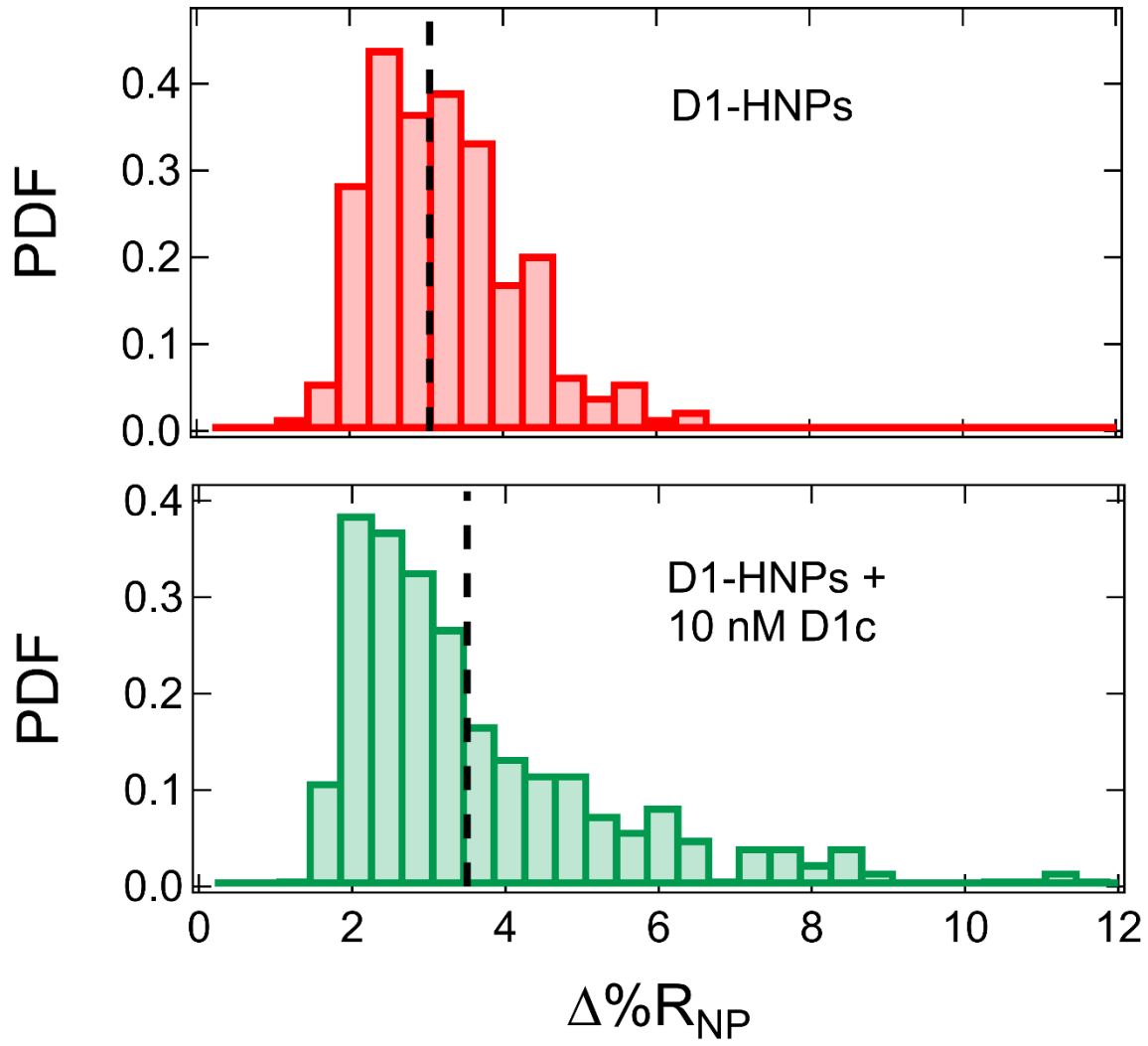

Figure A.3 Δ%R frequency distribution histogram obtained from the SPRI adsorption measurements of DNA-HNPs formed via Michael addition (red) and those nanoparticles exposed to 10 nM cDNA (green). The averages are 3.0 ± 0.12 and 3.50 ± 0.22%, respectively.